nature photonics

Article

https://doi.org/10.1038/s41566-023-01346-2

Plasmonic photoconductive terahertz focal-plane array with pixel super-resolution

In the format provided by the authors and unedited

Table of Content

Supplementary Text

Impact of the number of nanoantenna clusters on the performance of the FPA

For a given number of plasmonic nanoantennas, the number of clusters, $N_{clusters}$, determines both the SNR and space-bandwidth product (and also the spatial resolution within a given field-of-view) of the imaging system. The SNR of each cluster is calculated as $I_{ph}^2/\overline{i_n^2}$, where I_{ph} is the induced photocurrent in each cluster in response to an incident terahertz radiation and i_n is the noise current of each cluster, dominated by the Johnson-Nyquist noise. The induced photocurrent and noise current are proportional to P_{opt} and $P_{opt}^{1/2}$, respectively, where P_{opt} is the optical power pumping each cluster. For a uniform optical illumination across all the FPA nanoantennas, the optical power pumping each cluster is calculated as the total optical pump power divided by the number of clusters. Therefore, the SNR of each cluster is inversely proportional to the number of clusters, $SNR \propto 1/N_{clusters}$.

The number of clusters also determines the native space-bandwidth product of the FPA (unless a computational reconstruction method is used to further enhance it as we demonstrated in this work). Stated differently, the spatial resolution of the native terahertz imaging system within a given sample field-of-view is inversely proportional to (and gets better with) the number of clusters in each lateral direction. For the fabricated FPA with ~0.3 million plasmonic nanoantennas, the number of clusters was chosen to be 63 to provide a very high SNR for all the clusters (81 dB peak SNR) while maintaining an effective pixel number of 1-kilo pixels after the neural network-based PSR. Assuming that the total number plasmonic nanoantennas on the FPA is fixed/constant (e.g., 283,500 as used in this work), further increasing the number of clusters would improve the native space-bandwidth product of the FPA at the cost of an SNR degradation. However, a larger number of clusters can be achieved at the same SNR level (81 dB peak SNR) by further increasing the number of the plasmonic nanoantennas to e.g., >1 million, which is within the reach of the current fabrication methods to further scale-up the presented FPA technology in terms of its effective space-bandwidth product.

Impact of spectral bandwidth on the performance of the PSR network

The super-resolved thickness images shown in Fig. 2 of the main text and Supplementary Fig. S5 were computed by the associated convolutional neural networks (CNNs) that used the 41 amplitude channels of the spectral components within the band 0.5 THz – 1 THz. In addition, the 42nd channels at the input of these PSR networks representing the estimate of the thickness images were also computed based on the slope of the unwrapped phase within the same band. To select the optimal band for estimating the slope of the spectral phase and the amplitude channels fed into the convolutional PSR network architecture shown in Fig. 2, we relied on empirical evidence shown in Supplementary Figs. S9 and S10, respectively. In Supplementary Fig. S9, we compared the impact of the selected band of frequencies on the quality of the thickness image estimate computed based on the slope of the spectral phase in terms of squared-error (MSE) and SSIM computed with respect to the ground truth images. Although the behavior of SSIM and MSE exhibits a slightly different behavior as a function of bandwidth, a common trend is that slope-based material thickness estimation yields better results for both metrics as the spectral bandwidth utilized for fitting a line to the unwrapped phase increases. The MSE metric, on the other hand, shows a critical turning point for the band between 0.5 THz – 1.1 THz, where, contrary to the general trend, the inclusion of the components from 1 THz to 1.1 THz causes an increase in the error due to the water absorption lines located in the close vicinity of 1.1 THz. Therefore, we opted to use the spectral band between 0.5 THz and 1 THz to estimate the slope of the spectral phase which, in return, results in the estimated thickness images fed into the CNNs.

Next, we investigated the effect of the bandwidth covered by the amplitude channels on the PSR performance of our terahertz imaging system. Towards this goal, we swept the spectral bandwidth contributing to the input channels of the PSR neural network for the test set shown in Fig. 2 across 8 different candidates starting with the narrowest-band option 0.5 THz – 0.55 THz up to the widest using all the components within the range of 0.5 THz – 2.1 THz. For each of these candidate bandwidths, we trained a new PSR network from scratch and compared the quality of the super-resolved images in terms of both SSIM and PSNR as shown in Supplementary Fig. S10. Similar to the trend in Supplementary Fig. S9, both SSIM and PSNR improve as the bandwidth, thus the number of amplitude channels at the input of the convolutional network, increases up to the point, where all the spectral components between 0.5 THz and 1 THz are utilized. For instance, the deep neural network trained based on the smallest bandwidth considered in this analysis covering the range from 0.5 THz to 0.55 THz can only achieve 0.737±0.137 SSIM score and 13.08±5.09 dB PSNR value. These values point to a significantly inferior image reconstruction performance compared to the images shown in Fig. 2 for which the SSIM and PSNR were reported in the main text as 0.839±0.098 and 16.60±3.67 dB, respectively, highlighting the vital role of the broadband operation of our THz-FPA in achieving the super-resolution imaging task.

Numerical forward model of the lensless terahertz imaging setup

The terahertz numerical forward model represents the terahertz wave propagation and its interaction with the imaged objects, and generates the hyperspectral output images at the FPA plane corresponding to arbitrary objects. We formulated the terahertz forward model using the Rayleigh-Sommerfeld diffraction integral and the related angular spectrum representation of terahertz waves. Let $\boldsymbol{u}$ and $\boldsymbol{w}$ column vectors (N×1) represent the sampled terahertz fields (including the phase and amplitude information) at the input and output of a homogeneous medium, respectively. These two vectors are related through a matrix multiplication, $\boldsymbol{H}_{\boldsymbol{d},\boldsymbol{n},\boldsymbol{\lambda}}\boldsymbol{u} = \boldsymbol{w}$, where $\boldsymbol{H}_{\boldsymbol{d},\boldsymbol{n},\boldsymbol{\lambda}}$ is an N×N matrix that represents the Rayleigh-Sommerfeld diffraction between two fields specified over parallel planes, which are axially separated by a distance d. The subscripts n and λ denote the refractive index of the propagation medium and the wavelength of the diffracted terahertz wave, respectively. Since a homogeneous medium acts as a linear shift-invariant system, $\boldsymbol{H}_{\boldsymbol{d},\boldsymbol{n},\boldsymbol{\lambda}}$ is a Toeplitz matrix, and is diagonalizable by the 2D Fourier transform matrix, $\boldsymbol{F}$, i.e., $\boldsymbol{H}_{\boldsymbol{d},\boldsymbol{n},\boldsymbol{\lambda}} = \boldsymbol{F}^{-1}\boldsymbol{Q}_{\boldsymbol{d},\boldsymbol{n},\boldsymbol{\lambda}}\boldsymbol{F}$, and its eigenvalues (i.e., the diagonal elements of $\boldsymbol{Q}_{\boldsymbol{d},\boldsymbol{n},\boldsymbol{\lambda}}$), $q(\upsilon, \nu, d, n, \lambda)$, can be written as,

$$q(\upsilon, \nu, d, n, \lambda) = \begin{Bmatrix} exp\left[j2\pi \frac{nd}{\lambda}\sqrt{1-\left(\frac{\lambda}{n}\upsilon\right)^2-\left(\frac{\lambda}{n}\nu\right)^2}\right] & for\ \upsilon^2+\nu^2 \le \left(\frac{n}{\lambda}\right)^2 \\ 0 & otherwise \end{Bmatrix}. \quad \text{(S1)}$$

where, υ and ν denote the spatial frequencies.

The fabricated thickness patterns used in our experiments were etched over the surface of a 500-µm-thick silicon substrate and the volume between the back-surface of the silicon substrate and the active area of the THz-FPA is covered by a 680-µm-thick GaAs substrate. Therefore, the wave propagation in our terahertz forward model uses matrices $\boldsymbol{Q}_{\boldsymbol{d_{GaAs}},\boldsymbol{n_{GaAs}},\boldsymbol{\lambda}}$ and $\boldsymbol{Q}_{\boldsymbol{d_{Si}},\boldsymbol{n_{Si}},\boldsymbol{\lambda}}$ containing the eigenvalues of wave diffraction inside these two materials. Accordingly, the terahertz transfer function from the etched surface of the silicon substrate (i.e., the object plane) to the active area of the THz-FPA is given by $\boldsymbol{T}_{\boldsymbol{\lambda}} = \boldsymbol{F}^{-1}\boldsymbol{Q}_{\boldsymbol{d_{GaAs}},\boldsymbol{n_{GaAs}},\boldsymbol{\lambda}}\boldsymbol{Q}_{\boldsymbol{d_{Si}},\boldsymbol{n_{Si}},\boldsymbol{\lambda}}\boldsymbol{F}$. Since the maximum etch thickness, Δ_t, used in our experimental system is 40 µm that is much smaller than the wavelengths considered in our forward model (i.e., $\Delta_t \ll \lambda_k, for\ k = 1,2,3, \dots, N$), we modeled the object pattern, $\boldsymbol{t}[p, r]$, as a thin modulation surface. Consequently, for the sampled illumination beam at a given wavelength, $\boldsymbol{i}_{\boldsymbol{\lambda}}[p, r]$, incident over the etched surface of the silicon substrate with the etching pattern described by $\boldsymbol{t}[p, r]$, the outgoing, modulated beam is given by $\boldsymbol{o}_{\boldsymbol{\lambda}}[p, r] = \boldsymbol{i}_{\boldsymbol{\lambda}}[p, r]\exp(-j2\pi\frac{(n_{Si}-1)t[p,r]}{\lambda})$, where n_{Si} is the refractive index of silicon. n_{Si} and n_{GaAs} were assumed to be 3.42 and 3.6, respectively.

In our forward model, we represented the input thickness patterns and the associated terahertz fields at every plane with a sampling rate of 30 µm and 33.75 µm in the lateral dimensions, which correspond to 1/8th of the physical pixel size of our THz-FPA, 240µm×270µm. Stated differently, a given thickness pattern $\boldsymbol{t}[p,r]$ is represented through 56×72 pixels and each pixel was assumed to occupy an area of 30 μm×33.75 μm.

According to our forward model, for a thickness pattern $\boldsymbol{t}[p,r]$ of size 56×72 at any given wavelength, the corresponding complex-valued field measured by our THz-FPA can be written as $\boldsymbol{u_\lambda}[s'] = \boldsymbol{D}\boldsymbol{T_\lambda}'\boldsymbol{o_\lambda}[s]$, where $\boldsymbol{o_\lambda}[s]$ denotes the 1D vectorized counterpart of $\boldsymbol{o_\lambda}[p,r]$, i.e., $\boldsymbol{o_\lambda}[s] = vec(\boldsymbol{o_\lambda}[p,r])$. $\boldsymbol{T_\lambda}'$ is a (56×72)×(56×72) matrix obtained from the N×N terahertz transfer matrix $\boldsymbol{T_\lambda}$ described above by deleting the appropriately selected rows and columns. In our simulations N was taken as 512. $\boldsymbol{D}$ is a matrix of size (7×9)×(56×72) representing: (1) the integration of the complex-valued field samples over each pixel of the THz-FPA, and (2) the downsampling operator.

In order to expand the deep learning-based super-resolved material thickness estimation scheme presented in our paper and cover object patterns with multiple levels of etch depths and smaller contrast, we simulated the wave fields at 41 wavelengths from 0.5 THz to 1 THz created by 1092 different object patterns with non-binary depths and smaller contrast, using the above outlined numerical forward model. Out of these 1092 hyperspectral simulated object fields, we used 984 for transfer learning that further trained the neural network shown in Fig. 2a of the main text (originally trained only on the experimental data) to cover these new set of objects with multiple etch depths. During the transfer learning phase, the learning rate was set to be 200× smaller and the number of epochs was set to be 2.5× larger compared to the original training based solely on the experimental data. The remaining 108 simulated hyperspectral field data were reserved for blind testing to quantify the success of the transfer learning step and the resulting neural network model. Comparison of the predictions of our terahertz forward model against the experimental measurements are shown in Supplementary Fig. S17, demonstrating the agreement between the generated/simulated output images at the FPA plane and the corresponding experimental results.

Holographic reconstruction of the terahertz video frames

To reconstruct each frame of the terahertz video, we take advantage of the coherent wave detection capabilities of our THz-FPA. Specifically, since our THz-FPA can measure both the amplitude and phase of terahertz radiation at each pixel, we can holographically reconstruct the input objects. Hence, the problem of reconstructing an input object/scene reduces to inverting the terahertz wave transfer matrix between the complex-valued measurements, $\boldsymbol{u_\lambda}$, and the complex-valued object modulation function, $\boldsymbol{o_\lambda}$. Denoting the targeted super-resolution factor in our multi-wavelength holographic reconstruction procedure with α_{SR}, the wave transfer matrix, $\boldsymbol{A_\lambda}$, is of size (7×9)×(7α_{SR}×9α_{SR}), at a given wavelength, λ. $\boldsymbol{A_\lambda}$ can be described as $\boldsymbol{A_\lambda} = \boldsymbol{DT_\lambda}'$, where $\boldsymbol{D}$ is a matrix of size (7×9)×(7α_{SR}×9α_{SR}) representing: (1) the integration of complex-valued field samples over each pixel of our THz-FPA, and (2) the downsampling operator. The matrix $\boldsymbol{T_\lambda}'$, on the other hand, is the (7α_{SR}×9α_{SR})×(7α_{SR}×9α_{SR}) inner matrix of an N×N wave propagation matrix, $\boldsymbol{T_\lambda}$, which is defined as $\boldsymbol{T_\lambda} = \boldsymbol{F}^{-1}\boldsymbol{Q}_{\boldsymbol{d_{GaAs}},\boldsymbol{n_{GaAs}},\boldsymbol{\lambda}}\boldsymbol{Q}_{\boldsymbol{d_{tape}},\boldsymbol{n_{tape}},\boldsymbol{\lambda}}\boldsymbol{F}$. The diagonal matrices $\boldsymbol{Q}_{\boldsymbol{d_{GaAs}},\boldsymbol{n_{GaAs}},\boldsymbol{\lambda}}$ and $\boldsymbol{Q}_{\boldsymbol{d_{tape}},\boldsymbol{n_{tape}},\boldsymbol{\lambda}}$ contain the eigenvalues of wave propagation inside the 680-µm-thick GaAs substrate and 75-µm-thick sticky tape used in our setup. For the reconstructed video shown in Supplementary Video and Supplementary Fig. S21, the super-resolution factor, α_{SR}, was taken as 2 corresponding to 2×2, i.e., 4× increase in the space-bandwidth product of our THz-FPA. For any super-resolution factor greater than 1, α_{SR}>1, the $\boldsymbol{A_\lambda}$ is a fat matrix, in other words, it has more columns than rows. As a result, $\boldsymbol{A_\lambda}$ is not invertible. To be able to solve this holographic super-resolved image reconstruction problem, we constructed a larger matrix $\boldsymbol{A} = \begin{bmatrix} \boldsymbol{A_{\lambda_1}} \\ \boldsymbol{A_{\lambda_2}} \\ \cdots \\ \boldsymbol{A_{\lambda_8}} \end{bmatrix}$ of size (8×7×9)×(7α_{SR}×9α_{SR}) that contains the transfer matrices of 8 different spectral components from 0.4 THz to 1 THz. Similarly, a measurement vector, $\boldsymbol{u}$, was constructed as follows; $\boldsymbol{u} = \begin{bmatrix} \boldsymbol{u_{\lambda_1}} \\ \boldsymbol{u_{\lambda_2}} \\ \cdots \\ \boldsymbol{u_{\lambda_8}} \end{bmatrix}$ containing the complex-valued field measured by our THz-FPA for all these 8 wavelength components. The forward model of the system can be written as $\boldsymbol{Ao} = \boldsymbol{u}$, where $\boldsymbol{o}$ is the (7α_{SR}×9α_{SR})×1 vector containing the complex-valued object field. $\boldsymbol{A}$ contains more rows than columns which suggests that the solution that minimizes the function $f(o) = \|\boldsymbol{Ao} - \boldsymbol{u}\|^2$ can be solved using the pseudo-inverse of $\boldsymbol{A}$. However, despite being a tall matrix, $\boldsymbol{A}$ is an ill-conditioned matrix which inevitably amplifies the noise component in the measurement vector $\boldsymbol{u}$. Consequently, to reliably compute the solution that minimizes $f(o)$, we regularized the solution space. In this work, we achieved this by solving

$$f'(o) = \|\boldsymbol{Ao} - \boldsymbol{u}\|^2 + \rho\|\boldsymbol{o}\|_{TV} + \xi\|g(\angle\boldsymbol{o})\|_{TV} \quad \text{(S2)}$$

where $\|.\|_{TV}$ stands for the total-variation (TV) norm. In our algorithm, we used the isotropic definition of TV norm, $\|\boldsymbol{x}\|_{TV} = \sum_p \sum_r \sqrt{\left(\Delta_p^h\boldsymbol{x}\right)^2 + \left(\Delta_p^v\boldsymbol{x}\right)^2}$, with Δ_p^h and Δ_p^v denoting the horizontal and vertical (on the 2-D lattice) first-order local difference operators (omitting the boundary corrections) [55]. The function g represents a 2D phase unwrapping operator, which, in this work, was implemented based on [56]. For each frame of the video illustrating the water flow through the pipes, the solution of this equation was computed using the Two-step Iterative Shrinkage-Thresholding (TwIST) algorithm [57] with $\rho = 10^{-4}$ and $\xi = 3 \times 10^{-5}$, which determine the strength of the TV-norm regulation on the amplitude and phase-channels of the complex-valued amplitude of the object field, $\boldsymbol{o}$, respectively (see Eq. S2).

Supplementary Table

Ref.	Year	Object imaging	Laser amplifier	Laser optical pulse energy	Pulse energy for THz detection	Pulse energy for THz generation	Laser repetition rate	Peak SNR
[58]	1996	No	NS	NS	NS	NS	NS	NS
[59]	1997	Yes	Yes	4 µJ	NS	2 µJ	250 kHz	NS
[60]	1998	Yes	Yes	NS	NS	NS	NS	40 dB
[61]	2000	Yes	Yes	4 µJ	NS	NS	250 kHz	NS
[62]	2002	Yes	Yes	> 800 µJ	1.4 µJ	800 µJ	1 kHz	NS
[63]	2003	No	Yes	> 150 µJ	NS	150 µJ	1 kHz	NS
[64]	2004	No	Yes	> 140 µJ	NS	140 µJ	1 kHz	56.7 dB
[65]	2004	No	Yes	> 260 µJ	60 µJ	200 µJ	1 kHz	46.8 dB
[66]	2004	No	Yes	NS	NS	NS	1 kHz	NS
[67]	2005	Yes	Yes	> 575 µJ	75 µJ	500 µJ	1 kHz	34.0 dB
[68]	2005	Yes	Yes	NS	NS	NS	1 kHz	NS
[69]	2006	Yes	Yes	700 µJ	NS	NS	1 kHz	NS
[70]	2007	Yes	Yes	NS	NS	NS	1 kHz	NS
[71]	2009	Yes	No	25 nJ	3.4 nJ	17.1 nJ	76 MHz	40 dB
[72]	2009	Yes	Yes	900 µJ	10 µJ	890 µJ	1 kHz	46.8 dB
[73]	2009	Yes	Yes	650 µJ	NS	NS	1 kHz	46.0 dB
[74]	2010	Yes	Yes	> 510 µJ	10 µJ	500 µJ	1 kHz	NS
[75]	2010	Yes	Yes	800 µJ	NS	NS	1 kHz	NS
[76]	2010	Yes	Yes	800 µJ	NS	NS	1 kHz	45.1 dB
[77]	2011	Yes	No	25 nJ	NS	NS	76 MHz	NS
[78]	2011	Yes	Yes	4 mJ	NS	NS	1 kHz	40.0 dB
[79]	2011	Yes	Yes	4 mJ	NS	3.5 mJ	1 kHz	30.0 dB
[80]	2012	Yes	Yes	4 mJ	NS	NS	1 kHz	NS
[81]	2013	Yes	Yes	800 µJ	10 µJ	490 µJ	1 kHz	NS
[82]	2013	Yes	Yes	NS	350 µJ	NS	NS	NS
[83]	2016	Yes	Yes	4 mJ	NS	NS	1 kHz	48.5 dB
[84]	2019	Yes	Yes	900 µJ	20 µJ	880 µJ	1 kHz	NS
[85]	2022	Yes	Yes	4 mJ	NS	NS	1 kHz	NS
Our Work	2022	Yes	No	31.6 nJ	8.7 nJ	6.6 nJ	76 MHz	81.4 dB

Table S1 Specifications of the existing terahertz imaging systems without raster scanning through electro-optic detection and their comparison with the specifications of our imaging system (last row) based on a plasmonic photoconductive THz-FPA. The specifications listed as 'NS' are Not Specified in the listed references. The references that did not demonstrate object imaging, instead imaged the terahertz beam profile.

Supplementary Figures

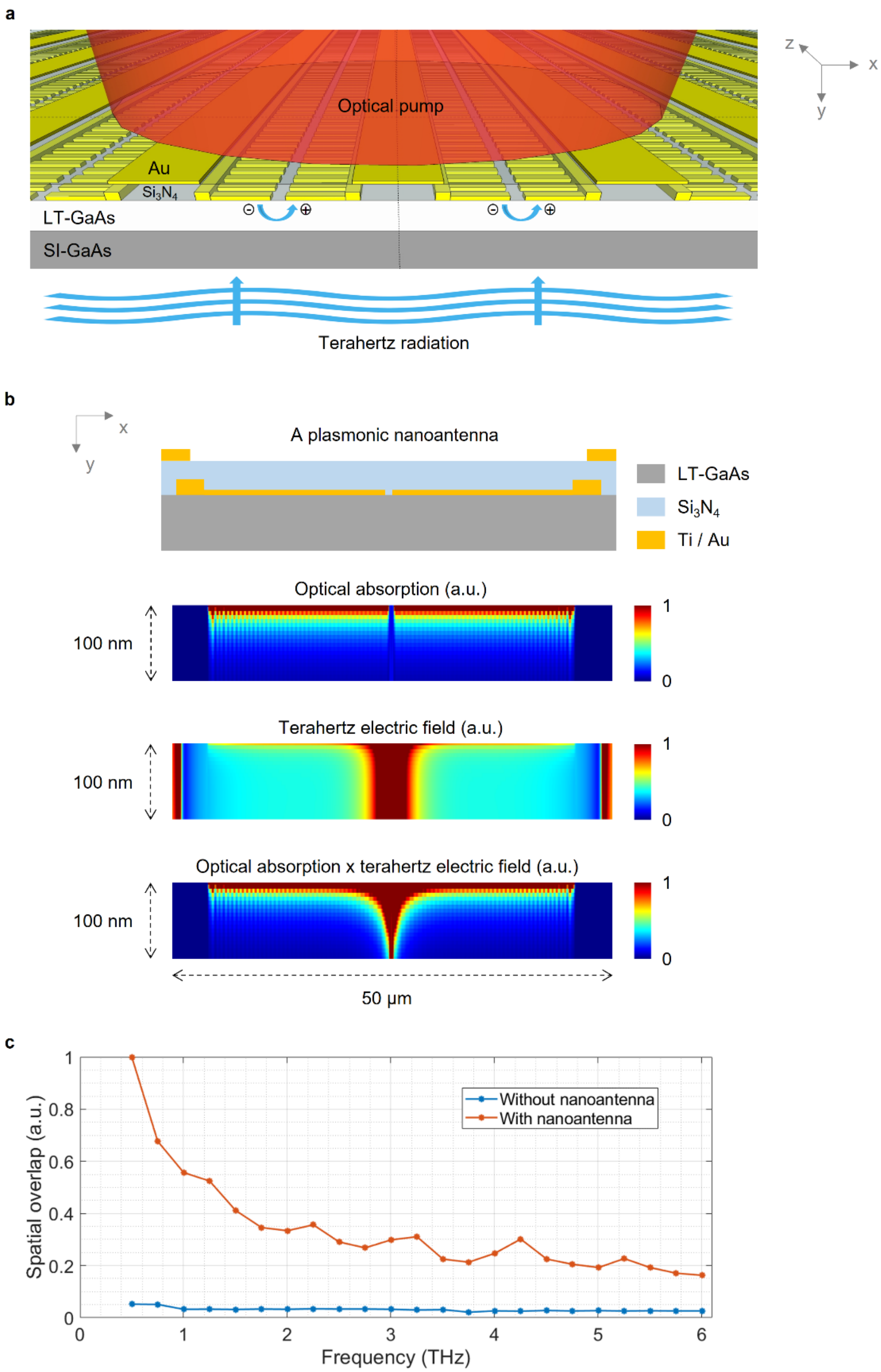

Figure S1 a, Schematic diagram of the THz-FPA based on a distributed plasmonic nanaoantenna array architecture. The geometry of the nanoantennas is chosen to obtain a strong spatial overlap between the received terahertz radiation and optical pump beam to achieve high detection sensitivity over a broad terahertz frequency range. **b,** The optical absorption profile (at λ = 800 nm), terahertz electric field profile (at f = 1 THz), and the multiplication product of the optical absorption and terahertz electric field profiles within a 100 nm depth in the LT-GaAs substrate. **c,** Spatial overlap between the optical and terahertz beams as a function of terahertz frequency with and without the plasmonic nanoantennas, which is defined as the integral of the multiplication product of the optical absorption and terahertz electric field under the nanoantennas. The distributed plasmonic nanaoantenna array architecture for the THz-FPA provides a much higher optical fill factor (49.1% for the demonstrated THz-FPA) compared to conventional photoconductive terahertz antenna arrays (less than 1%). In conventional photoconductive terahertz antennas, small optical active areas are connected to much larger discrete terahertz antenna elements (e.g., dipole, bow-tie, and spiral antennas), leading to a low optical fill factor when used in arrays. Since the detected terahertz power has a quadratic dependence on the optical pump power incident on the device active area, which is proportional to the optical fill factor, our THz-FPA provides significantly higher SNR (81 dB peak SNR) and broader bandwidth compared to conventional photoconductive terahertz antenna arrays with discrete terahertz antenna elements [86, 87]. To provide a high optical fill factor, the THz-FPA does not require any special focusing optics (e.g., microlens arrays, fiber bundles, or diffractive elements), making this distributed plasmonic nanoantenna array architecture scalable for large-pixel-count THz-FPAs.

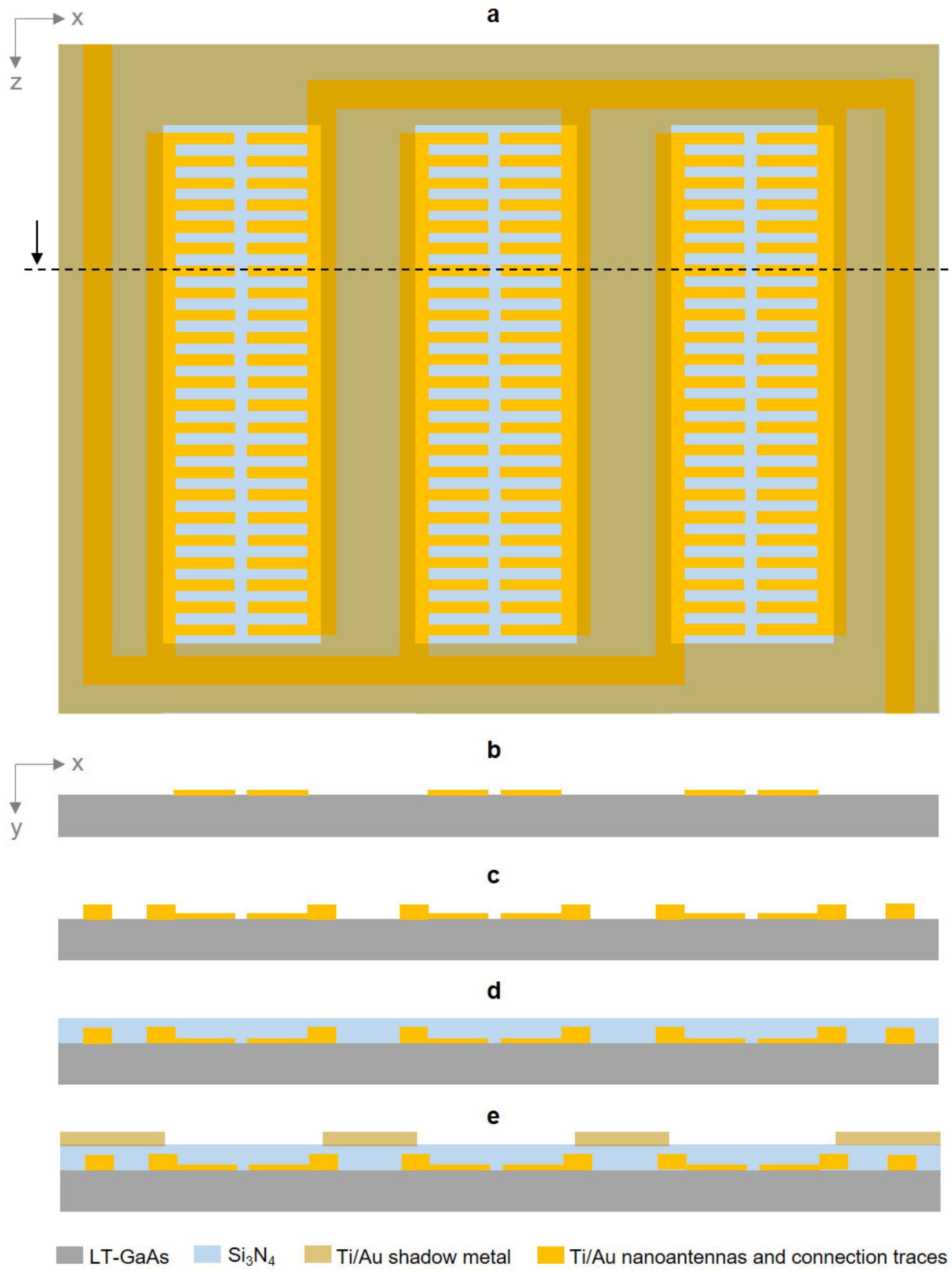

Figure S2 Fabrication process of the THz-FPA. **a,** The top-view of one cluster composed of plasmonic nanoantenna arrays. The fabrication process steps at the cross-section marked by the dashed line are illustrated in **b**-**e**. **b,** Starting with a low-temperature-grown GaAs (LT-GaAs) substrate and patterning the plasmonic nanoantennas using electron-beam lithography, followed by metal deposition (3/47-nm Ti/Au) and lift-off. **c,** Patterning connection traces and contact pads through photolithography, followed by metal deposition (20/180-nm Ti/Au) and lift-off. **d,** Depositing a 290-nm-thick silicon nitride anti-reflection coating through plasma-enhanced chemical vapor deposition. **e,** Patterning shadow metals through photolithography, followed by metal deposition (10/90-nm Ti/Au) and lift-off.

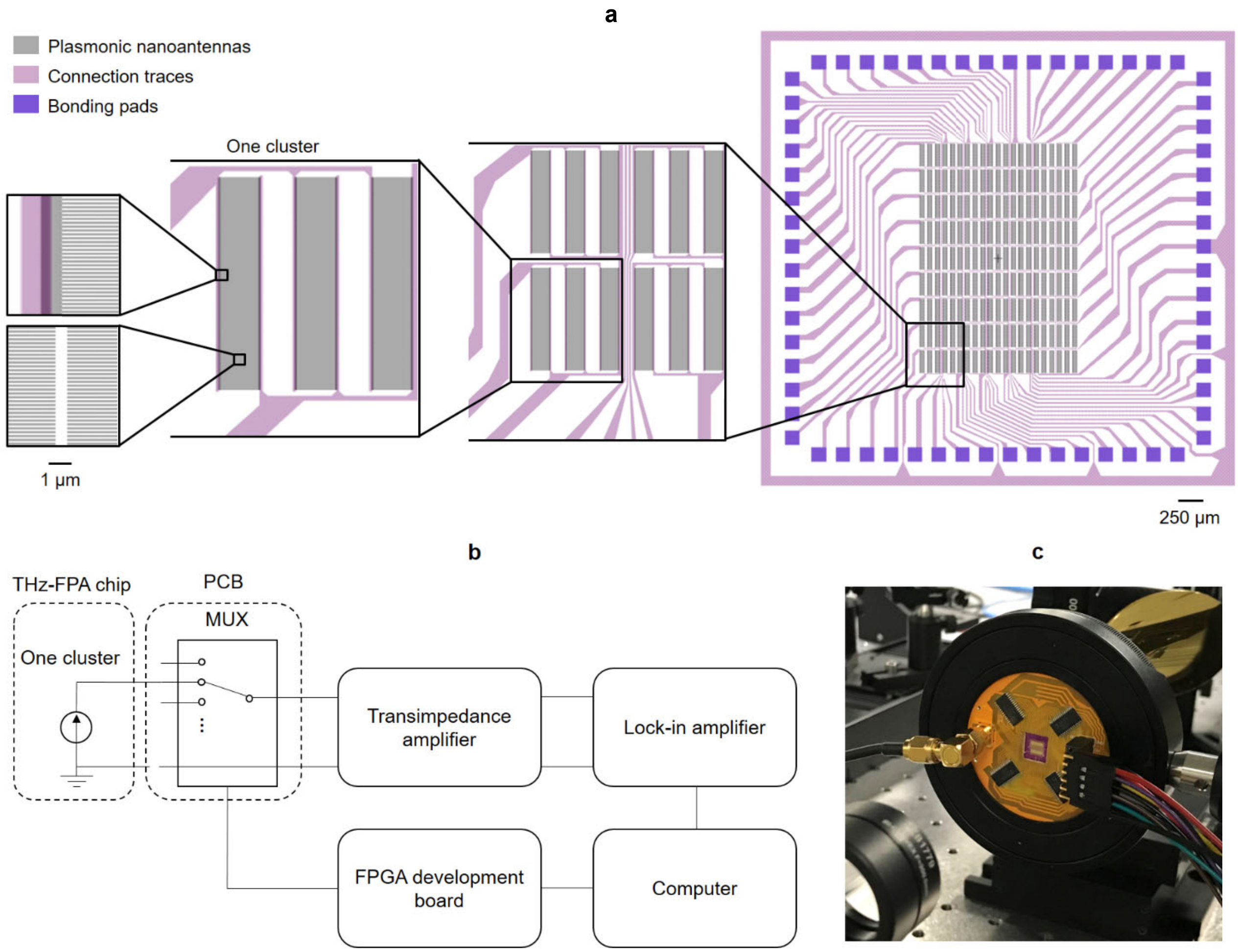

Figure S3 a, Layout of the THz-FPA, showing the plasmonic nanoantennas, connection traces, and bonding pads. A shadow metal layer (not shown in this layout) covers all the connection traces such that only the plasmonic nanoantennas are optically illuminated. **b**, Block diagram of the data acquisition system, which consists of an FPGA development board controlling four 16-channel multiplexers to route the FPA outputs to a transimpedance amplifier and lock-in amplifier sequentially. **c,** Photograph of the packaged THz-FPA in the imaging setup.

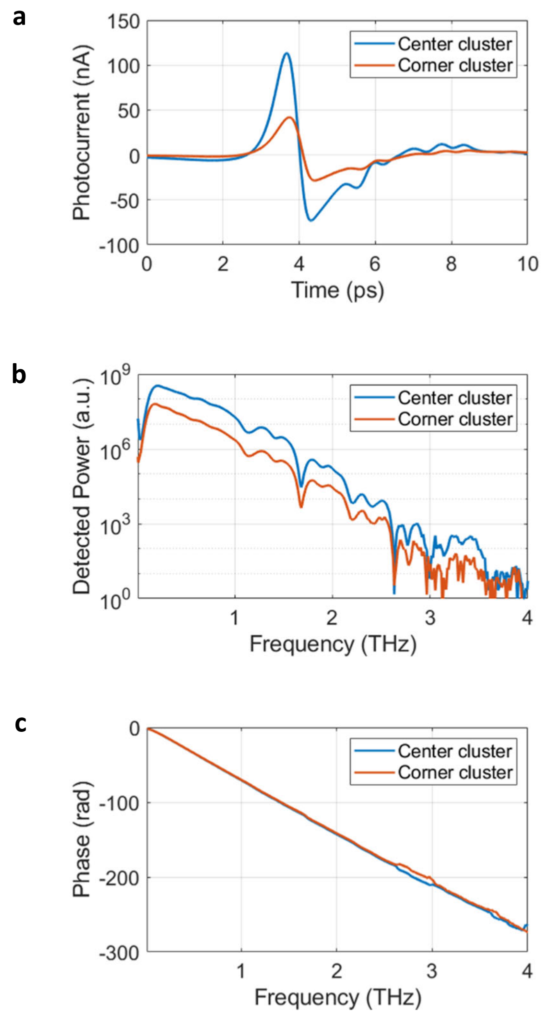

Figure S4 The time-domain electric field, frequency-domain power spectra, and frequency-domain unwrapped phase measured at a center pixel and a corner pixel of the THz-FPA are shown in **a**, **b**, and **c** respectively.

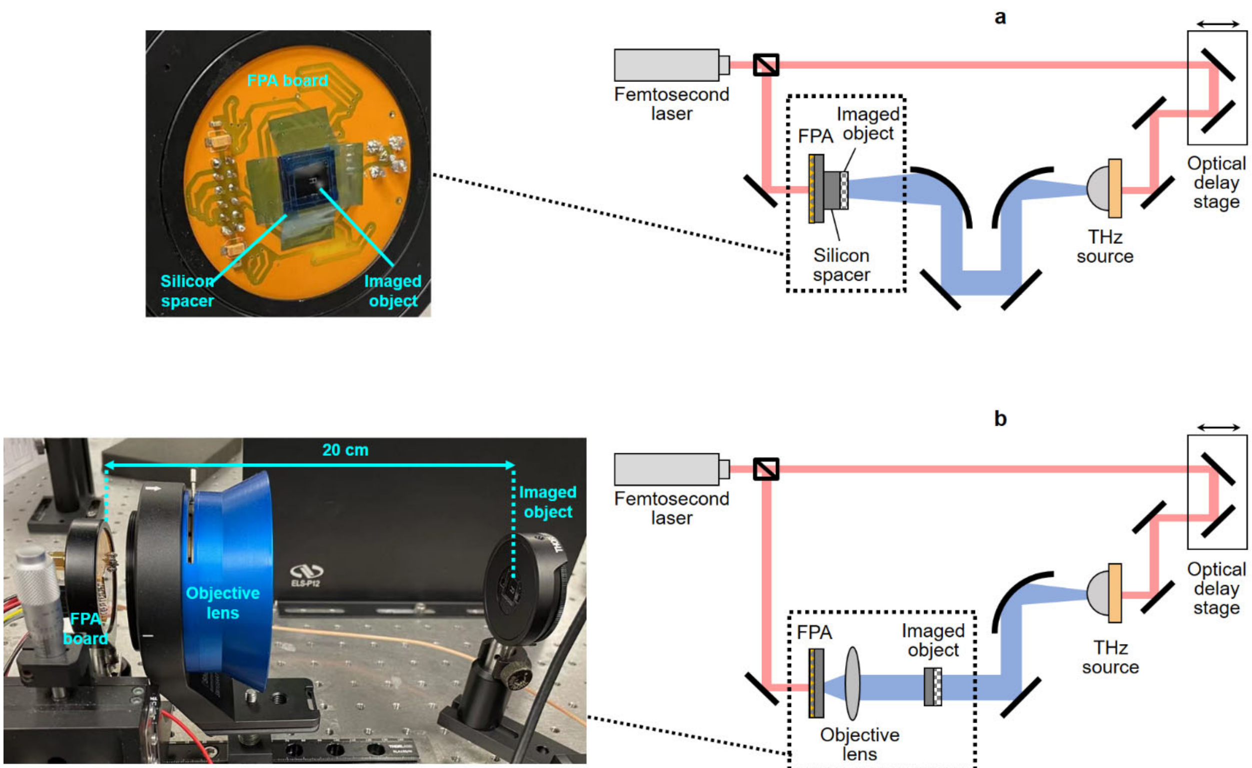

Figure S5 Block diagrams of two experimental setups used for terahertz time-domain imaging using our THz-FPA. **a,** The imaged objects are placed at a 1.1 mm axial distance from the active area of the THz-FPA using a high resistivity silicon substrate, which serves as a spacer. The 1.1 mm distance translates to 9.4 effective wavelengths at the median wavelength of 398 µm. Two parabolic mirrors are used to collimate and focus the terahertz radiation onto the THz-FPA after interacting with the imaged object. **b,** The imaged objects are placed at a 20 cm axial distance from the active area of the THz-FPA. One parabolic mirror and one objective lens (TeraLens, Lytid) are used to collimate and focus the terahertz radiation onto the THz-FPA after interacting with the imaged objects while providing a demagnification factor of ~2.76.

Figure S6 Raw spectral images of 'U', 'C', 'L', and 'A' patterns created in a 65 μm-thick copper plate captured by the fabricated THz-FPA over a 0.6-2.5 THz frequency range [88]. The minimum aperture width of all the patterns is 160 μm. The image resolution is degraded at lower frequencies due to the diffraction limit. The image quality also degrades at frequencies close to the water vapor absorption lines, 1.1 THz, 1.7 THz, 2.2 THz, and 2.4 THz, due to the high signal attenuation.

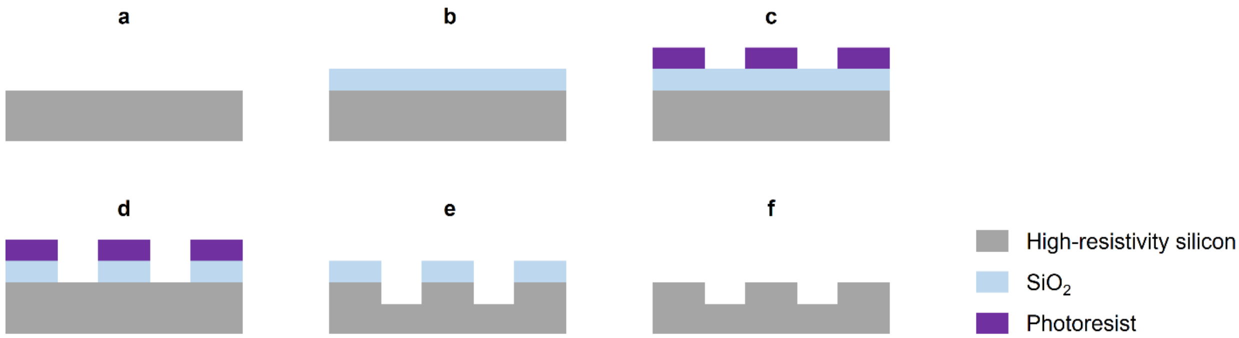

Figure S7 Fabrication process of the phase imaging objects. **a,** Starting with a high-resistivity silicon substrate. **b,** Growing a thermal oxide layer on the substrate. **c,** Defining the image patterns through photolithography. **d,** Forming a hard etch mask by dry etching the silicon dioxide layer. **e,** Forming the final image patterns by etching silicon through deep reactive-ion etching. **f,** Removing the silicon dioxide hard mask through buffered oxide etching.

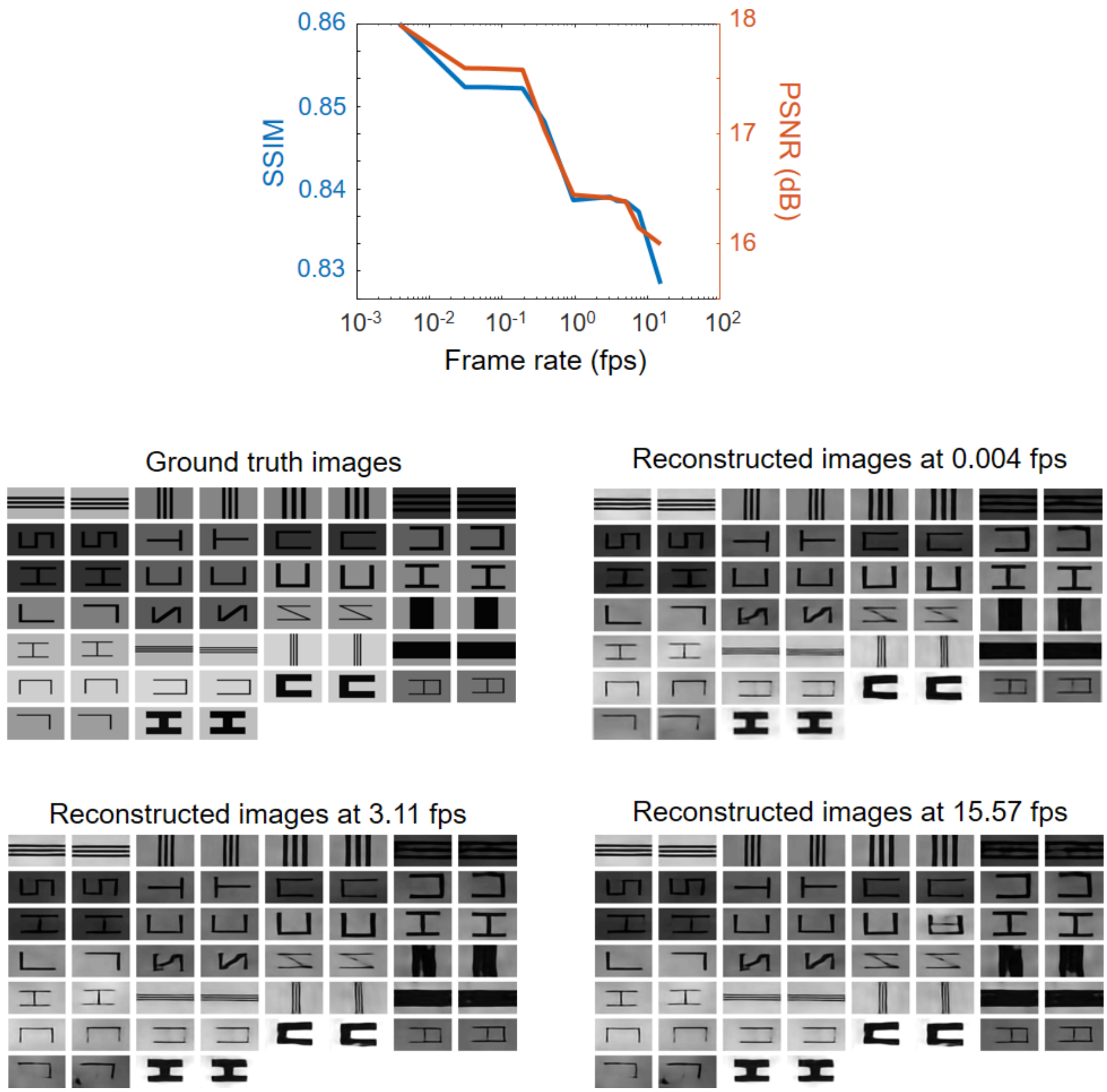

Figure S8 The speed of the THz-FPA imaging system for capturing the time-domain data from all the plasmonic clusters depends on (1) the speed and range of the optical delay stage used to vary the optical path difference between the optical pump and terahertz beams incident on the THz-FPA, (2) the number of the time-domain traces that are captured and averaged to resolve each image, and (3) the data acquisition scheme. By setting the speed and range of the optical delay stage to 50 mm/s and 25 mm, respectively, and capturing 8 time-domain traces for each image, we achieve an imaging speed of 0.004 fps. In this setting, one time-domain trace from each selected cluster is fully captured while moving the optical delay stage over a 25 mm range, before selecting another cluster and repeating the same data capture. The imaging speed can be significantly increased if the time-domain data from all clusters are captured sequentially while moving the optical delay stage over a 25 mm range. Through this data acquisition approach, the frame-rate is increased to 3.11 fps when reducing the optical delay stage range to 2.5 mm and capturing 5 time-domain traces for each image. Under this condition, reducing the number of the captured time-domain traces to 1 further increases the frame-rate to 15.57 fps. The depth and shape of all imaged objects are successfully resolved when effectively increasing the frame-rate from 0.004 fps to 15.57 fps with a small reduction in the image reconstruction SSIM (from 0.86 to 0.83) and PSNR (from 18 to 16 dB). The capability of the THz-FPA in offering fast imaging speeds enabled us to capture a dynamic video of water flow in adjacent plastic pipes at 16 fps (see the Supplementary Video).

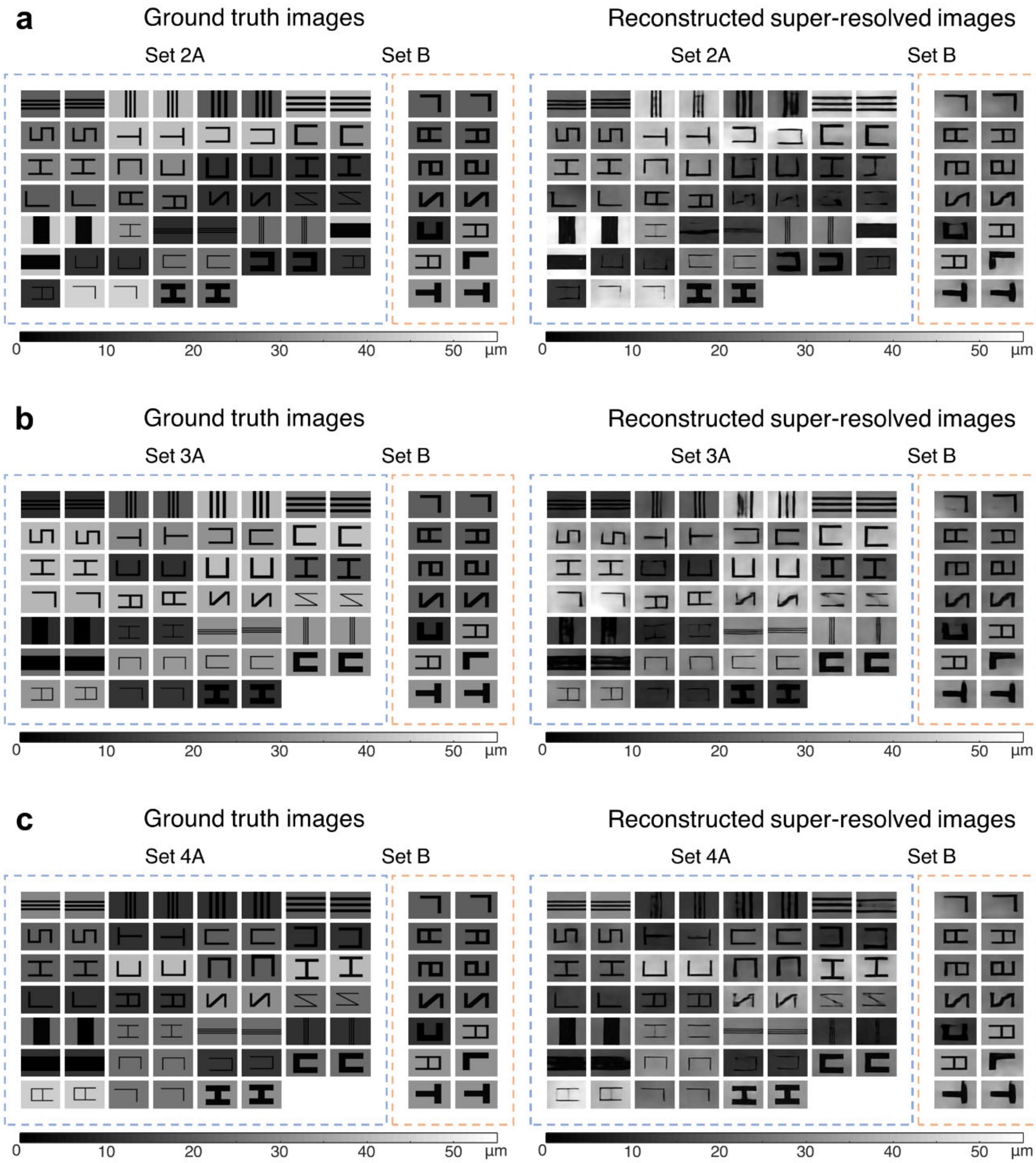

Figure S9 Generalization performance of the presented PSR-enhanced THz-FPA on different test sets: Sets 2A, 3A, and 4A shown in **a**, **b**, and **c**, respectively. The CNN architecture shown in Fig. 2 of the main text was trained from scratch to test on these 3 different datasets, where the training/testing partition of the image data is different for each case (see Methods section of the main text).

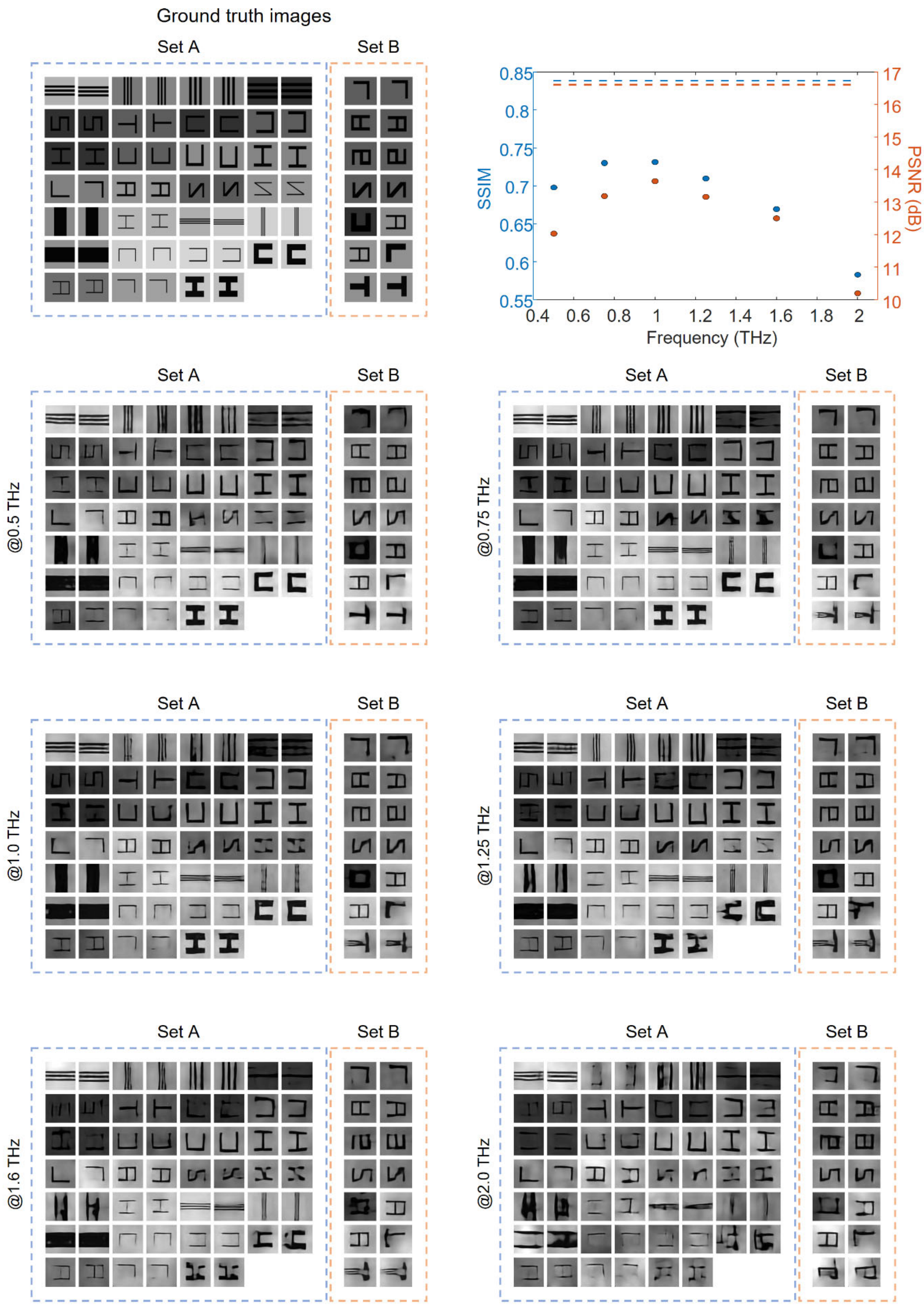
Ground truth images
Set A
Set B
SSIM
PSNR (dB)
Frequency (THz)
0.85
0.8
0.75
0.7
0.65
0.6
0.55
17
16
15
14
13
12
11
10
0.4
0.6
0.8
1
1.2
1.4
1.6
1.8
2
@0.5 THz
@0.75 THz
@1.0 THz
@1.25 THz
@1.6 THz
@2.0 THz

Figure S10 Single-frequency super-resolution networks and their comparison with our multi-spectral PSR-enhanced THz-FPA results. Ground-truth thickness images in the test set that are identical to the ones shown in Fig. 2 of the main text are shown on the top-left. There are six CNNs separately trained to perform PSR solely based on the amplitude and phase channel of a single spectral component at, 0.5 THz, 0.75 THz, 1.0 THz, 1.25 THz, 1.6 THz and 1.8 THz. The SSIM (blue) and PSNR (red) values achieved by these single-frequency PSR networks are depicted in the graph shown on the top-right, whereas the dashed lines represent the corresponding values attained by the multi-spectral PSR-enhanced THz-FPA results presented in the Fig. 2 of the main text.

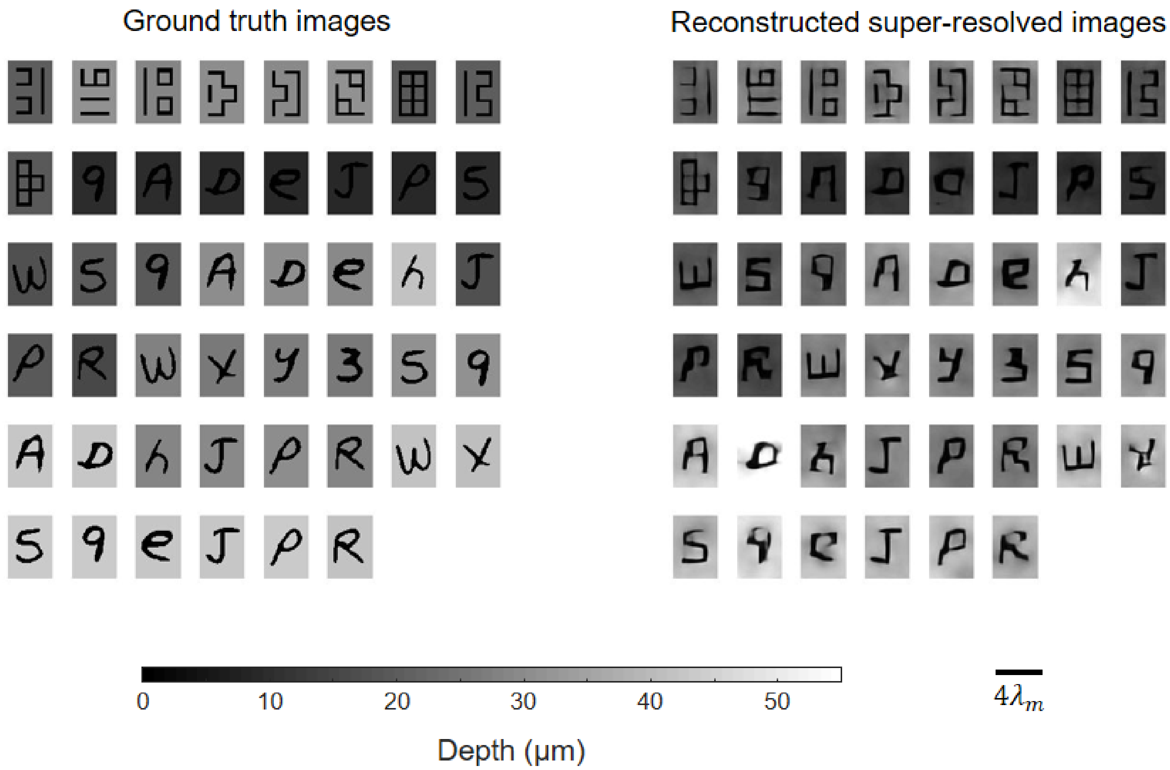

Figure S11 The ground truth and the reconstructed images of complex and irregular patterns, including hand-written numbers and letters, that were fabricated and etched in silicon. These objects are blindly tested with the same PSR neural network used in Fig. 2. No patterns with similar shapes were seen by the neural network during its training. The depth and shape of the patterns are successfully reconstructed with an average PSNR of 12 dB and SSIM of 0.64, confirming the generalization performance of the presented PSR-enhanced THz-FPA.

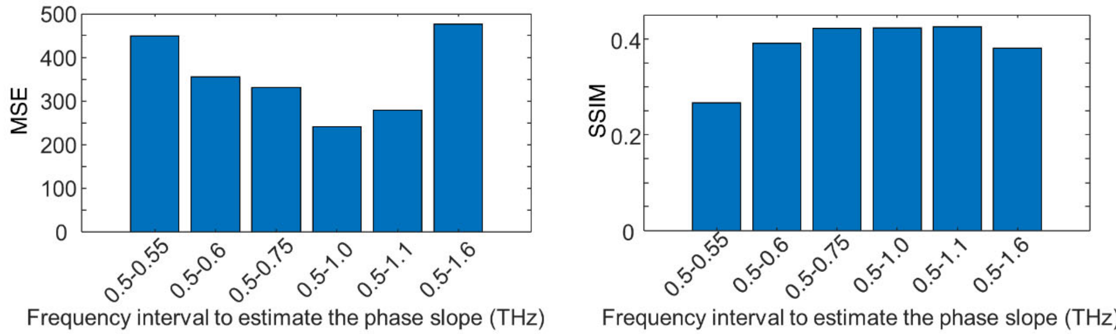

Figure S12 The impact of the spectral bandwidth on the quality of the thickness image estimate. Mean-square-error (MSE) (left) and Structural Similarity Index Measure (SSIM) (right) of the thickness image recovered using the slope of the unwrapped phase of the spectral components within different bands. Note that these metrics are not calculated based on the output of the PSR network, unlike e.g., the SSIM metrics reported in Fig. 4 of the main text. The band from 0.5 THz to 1 THz was found to be optimal, since it provides the lowest MSE. The reason behind the increasing MSE with the inclusion of the components beyond 1 THz is the existence of water absorption lines.

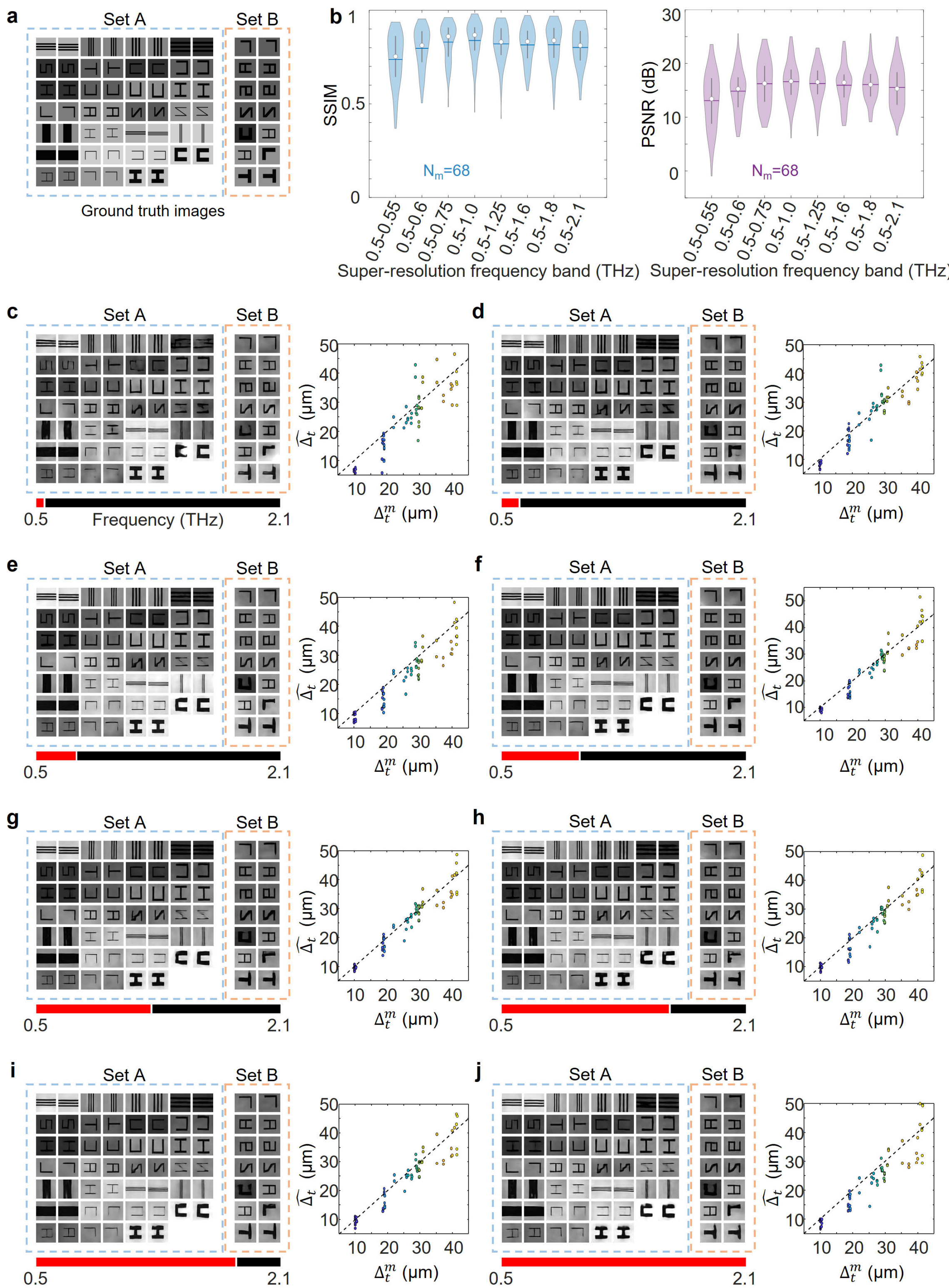

Figure S13 The impact of the spectral bandwidth on the presented PSR network inference. **a,** Ground-truth thickness images in the test set that is identical to the one shown in Fig. 2 of the main text. Eight different CNNs were separately trained and tested on this test set each performing PSR based on a different spectral band. **b,** Violin plots of SSIM (left) and PSNR (right) values of the super-resolved images illustrated in c-j. The horizontal line in each violin plot shows the mean value. The box plot inside each violin plot indicates the interquartile range, and the dot denotes the median value. N_m represents the sample size for each test set. **c-j,** The super-resolved images at the output layer of the PSR networks (left) and the associated thickness contrast estimation (right) when the PSR network was trained and tested based on the spectral components within the bands (c) 0.5 THz – 0.55 THz, (d) 0.5 THz – 0.6 THz, (e) 0.5 THz – 0.75 THz, (f) 0.5 THz – 1.0 THz, (g) 0.5 THz – 1.25 THz, (h) 0.5 THz – 1.6 THz, (i) 0.5 THz – 1.8 THz and (j) 0.5 THz – 2.1 THz. The super-resolved images shown in (f) are identical to the ones shown in Fig. 2 of the main text.

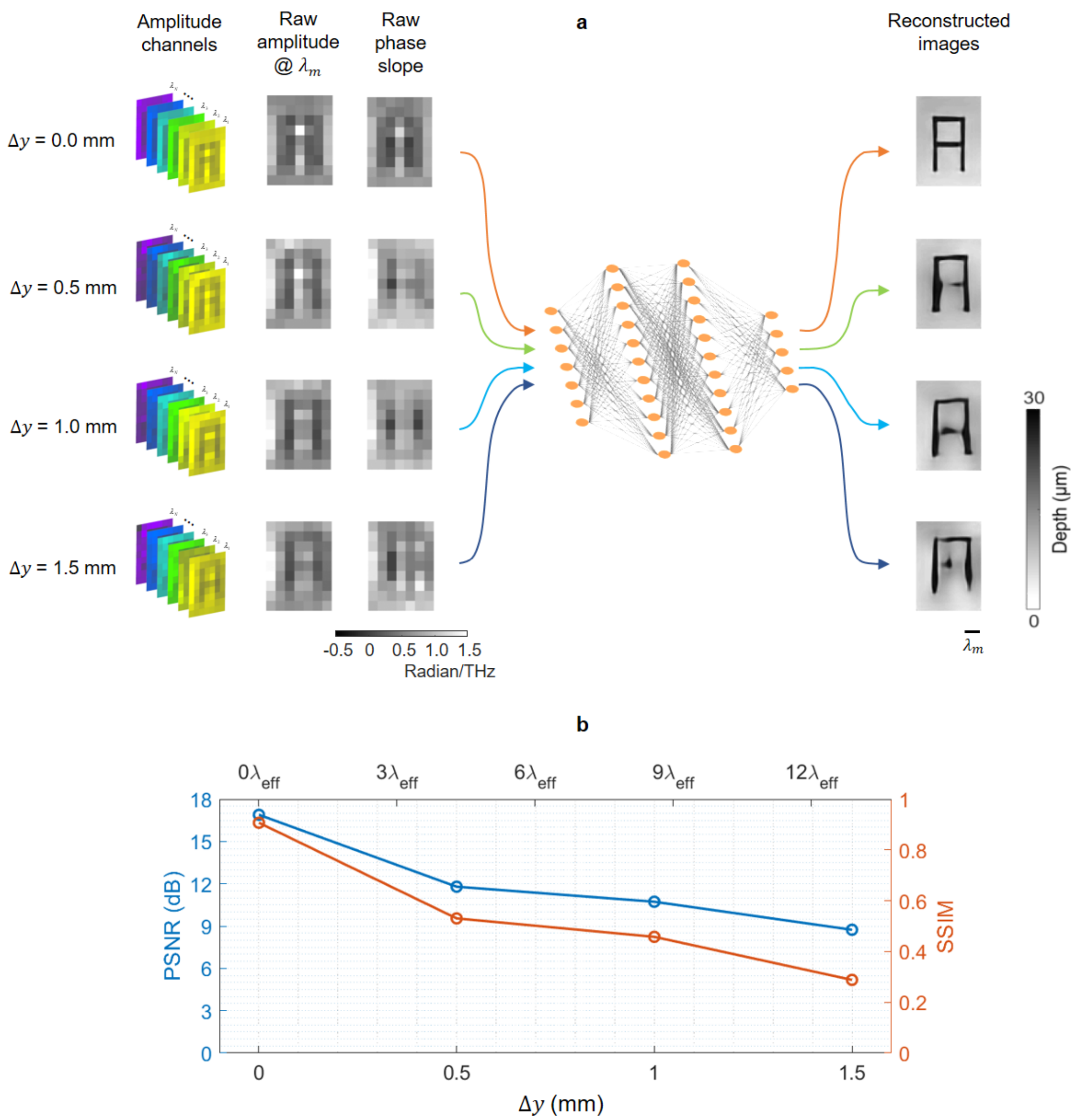

Figure S14 Depth-of-field analysis for the PSR-enhanced THz-FPA imaging system (shown in Fig. S5a). By increasing the number of silicon spacers placed between the imaged object and the THz-FPA, the axial distance of the object from the THz-FPA is experimentally increased by different Δy values. **a**, Reconstructed images for different axial displacements Δy = 0, 0.5, 1, and 1.5 mm. Although all the neural network training is performed for imaged objects placed at the 1.1 mm axial distance, the shape and depth of the object are successfully reconstructed for axial displacements as large as 1.5 mm (which is equivalent to 12.8 effective wavelengths at the median frequency of 0.754 THz). **b**, The PSNR and SSIM of the reconstructed images at different axial displacements.

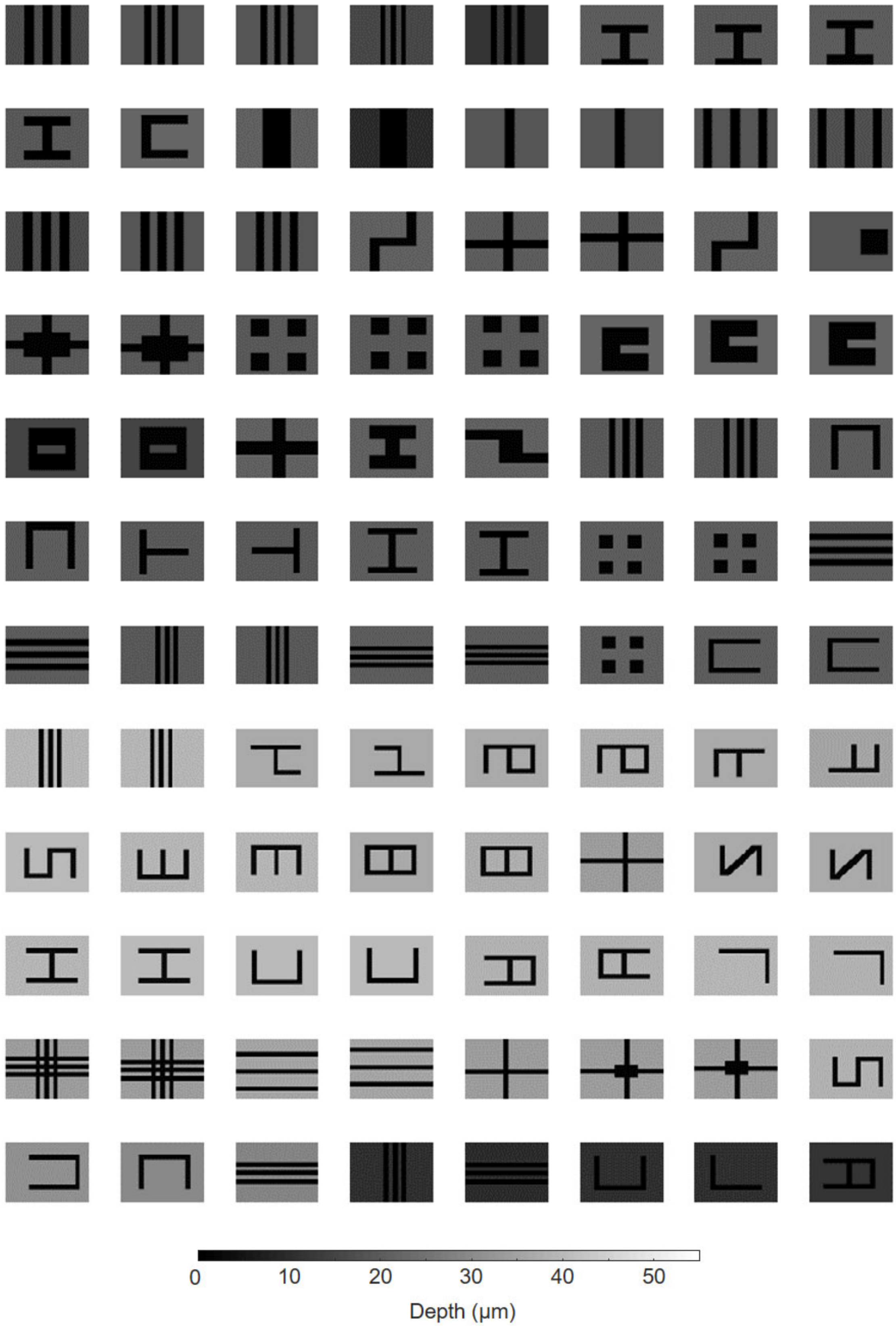

Figure S15 (1/3) Ground truth thickness images of the training set for the PSR neural network reported in Fig. 2.

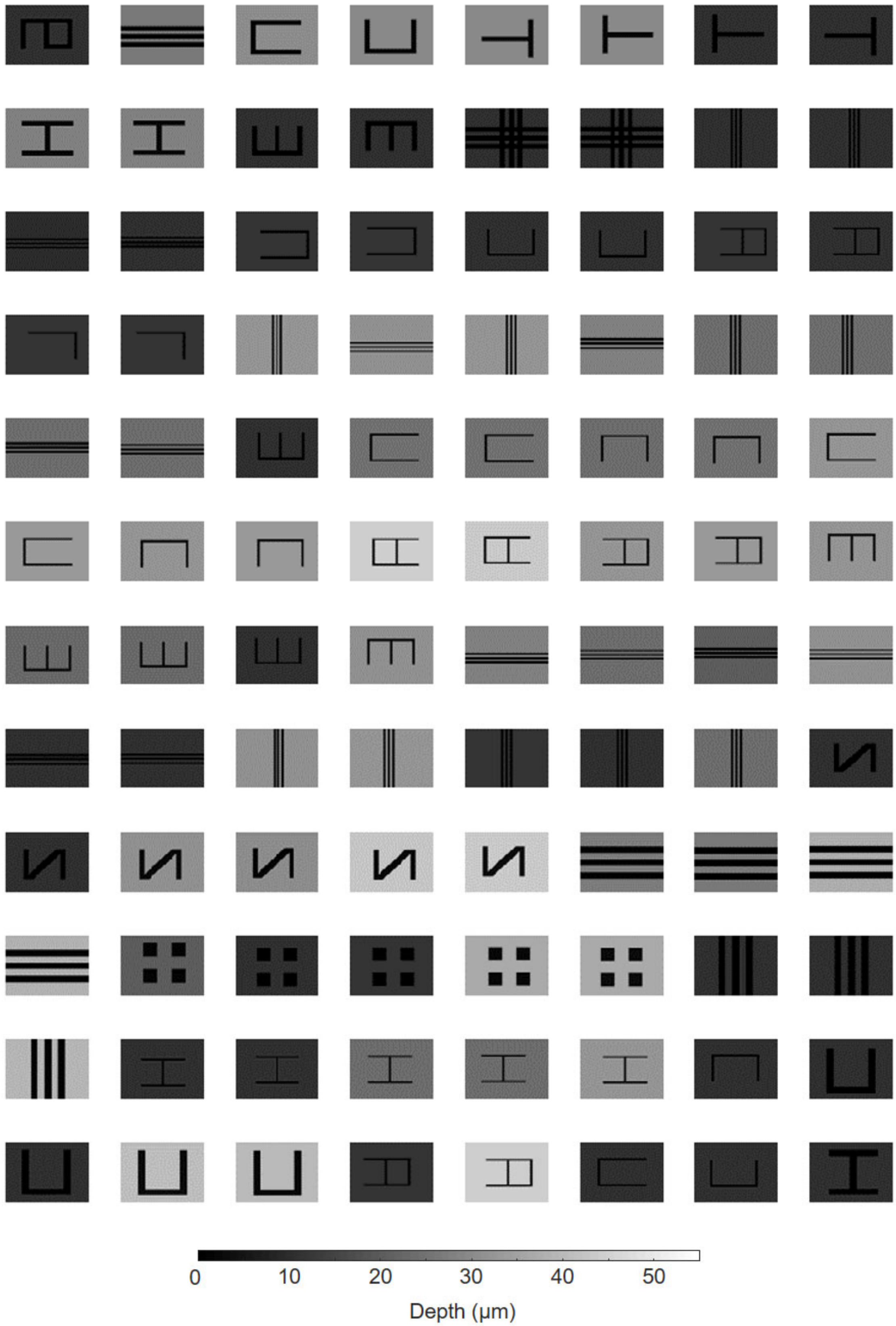

Figure S15 (2/3) Ground truth thickness images of the training set for the PSR neural network reported in Fig. 2.

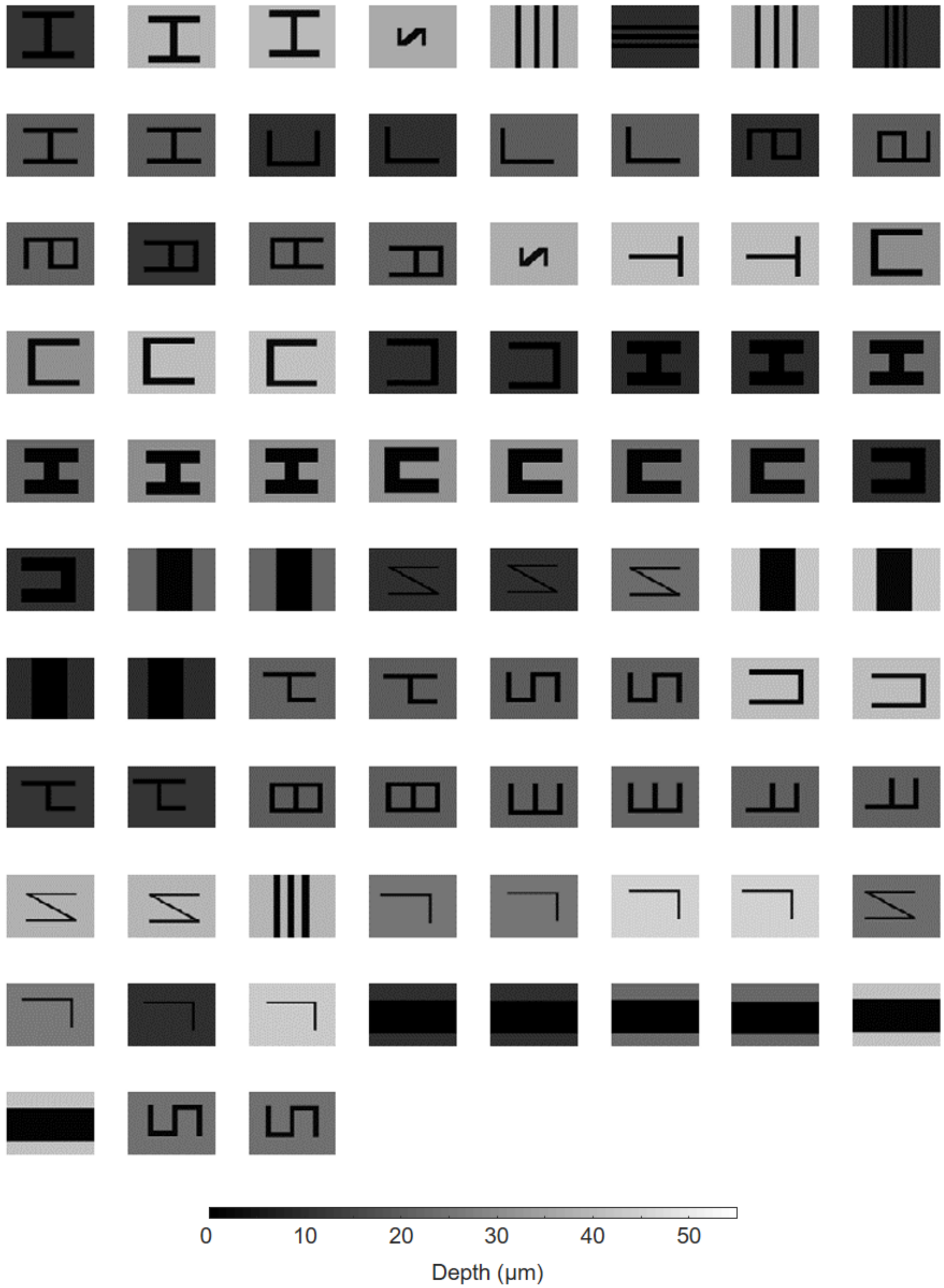

Figure S15 (3/3) Ground truth thickness images of the training set for the PSR neural network reported in Fig. 2.

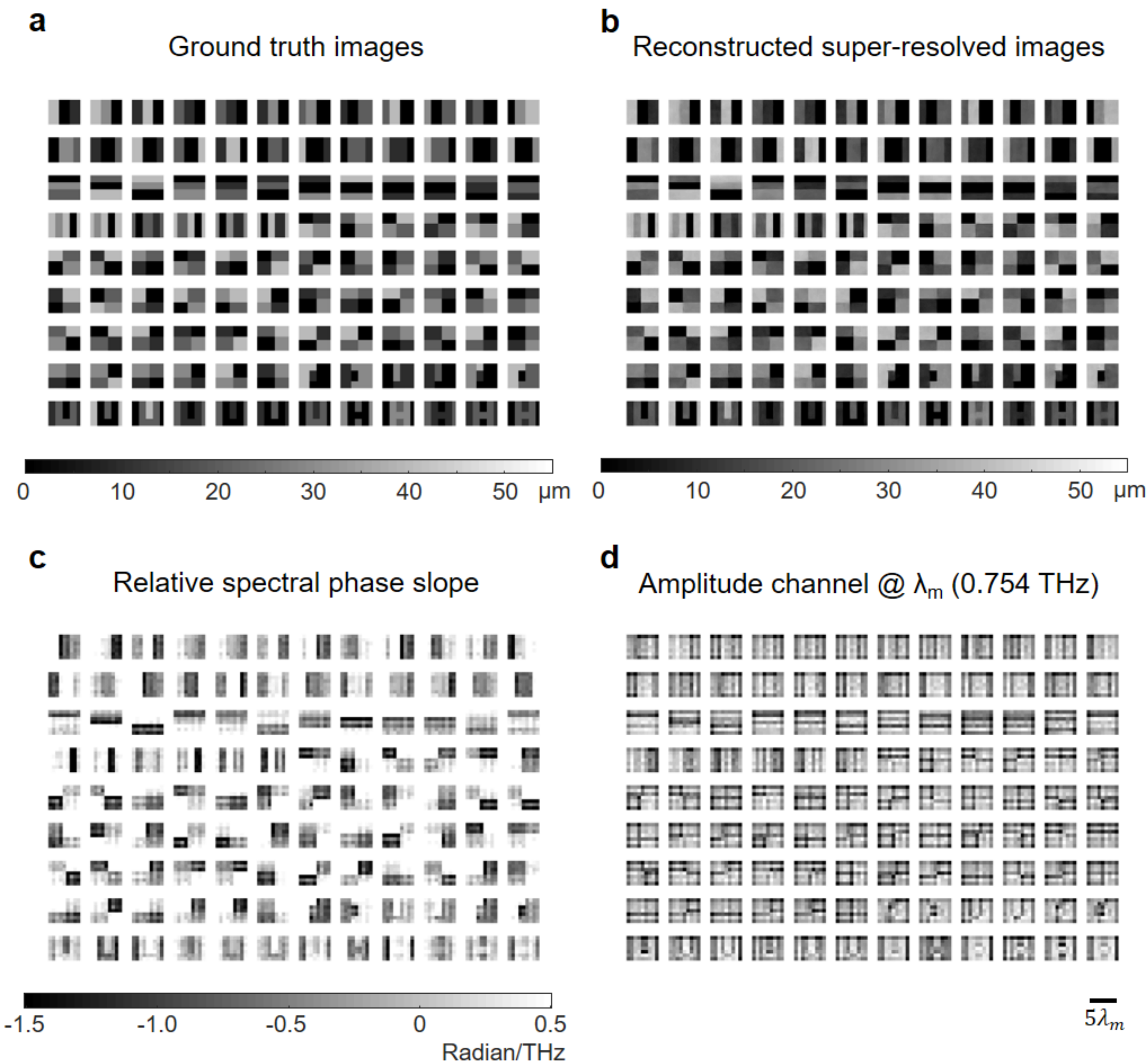

Figure S16 PSR-enhanced THz-FPA imaging with the capability of resolving objects with non-binary depths and smaller contrast. The original PSR neural network is enhanced by transfer learning using synthetic image data generated by a terahertz forward model (see the Supplementary Methods). **a,** Ground truth thickness images of the tested objects. **b,** Super-resolved images using the transfer-learned-PSR-enhanced THz-FPA. **c,** The relative spectral phase slope of the objects computed based on the slope of the unwrapped spectral phase distribution. **d,** The amplitude channel at the median frequency, f_m = 0.754 THz. The depth and shape of the patterns are successfully reconstructed with a PSNR of 29.4 dB and SSIM of 0.93, confirming the success of the transfer-learned, PSR-enhanced THz-FPA imaging system.

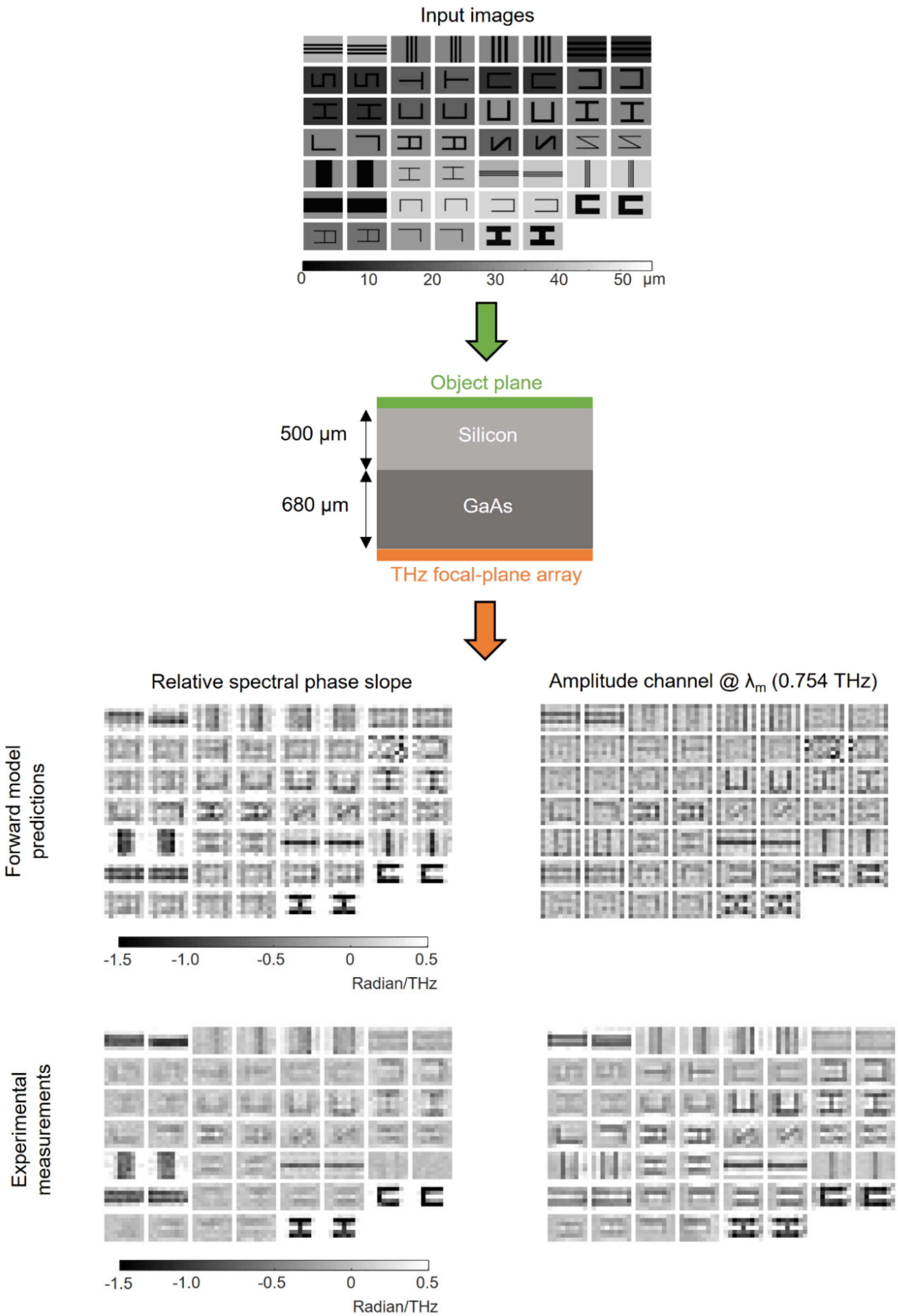

Figure S17 Comparison of the predictions of the terahertz wave forward model against the experimental measurements, demonstrating the agreement between the generated output terahertz signals at the FPA plane and the corresponding experimental results.

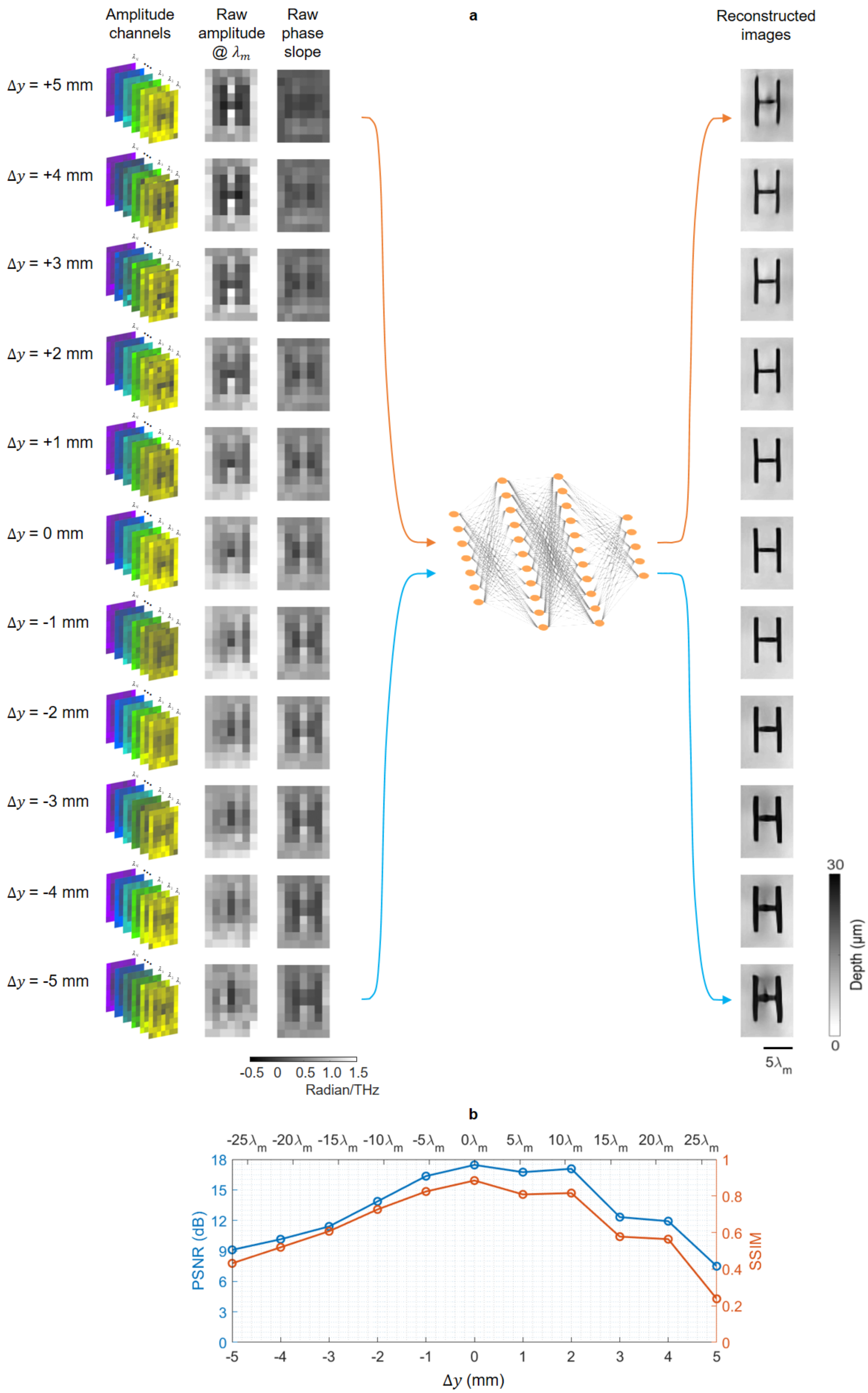

a
Amplitude channels
Raw amplitude @ λ_m
Raw phase slope
Reconstructed images
Δy = +5 mm
Δy = +4 mm
Δy = +3 mm
Δy = +2 mm
Δy = +1 mm
Δy = 0 mm
Δy = -1 mm
Δy = -2 mm
Δy = -3 mm
Δy = -4 mm
Δy = -5 mm
-0.5 0 0.5 1.0 1.5
Radian/THz
30
Depth (μm)
0
$5\lambda_m$
b
$-25\lambda_m$ $-20\lambda_m$ $-15\lambda_m$ $-10\lambda_m$ $-5\lambda_m$ $0\lambda_m$ $5\lambda_m$ $10\lambda_m$ $15\lambda_m$ $20\lambda_m$ $25\lambda_m$
PSNR (dB)
SSIM
Δy (mm)

Figure S18 Depth-of-field analysis for the PSR-enhanced THz-FPA imaging system (shown in Fig. S5b). **a**, Reconstructed images for different axial experimental displacements, Δy, ranging from -5 mm to 5 mm. Although all the neural network training is performed for imaged objects placed at the 20 cm axial distance, the shape and depth of the object are successfully reconstructed for axial displacements as large as 10 mm (which corresponds to an axial distance of 53.3 wavelengths at the median frequency of 1.6 THz). **b**, The PSNR and SSIM of the reconstructed images at different axial displacements.

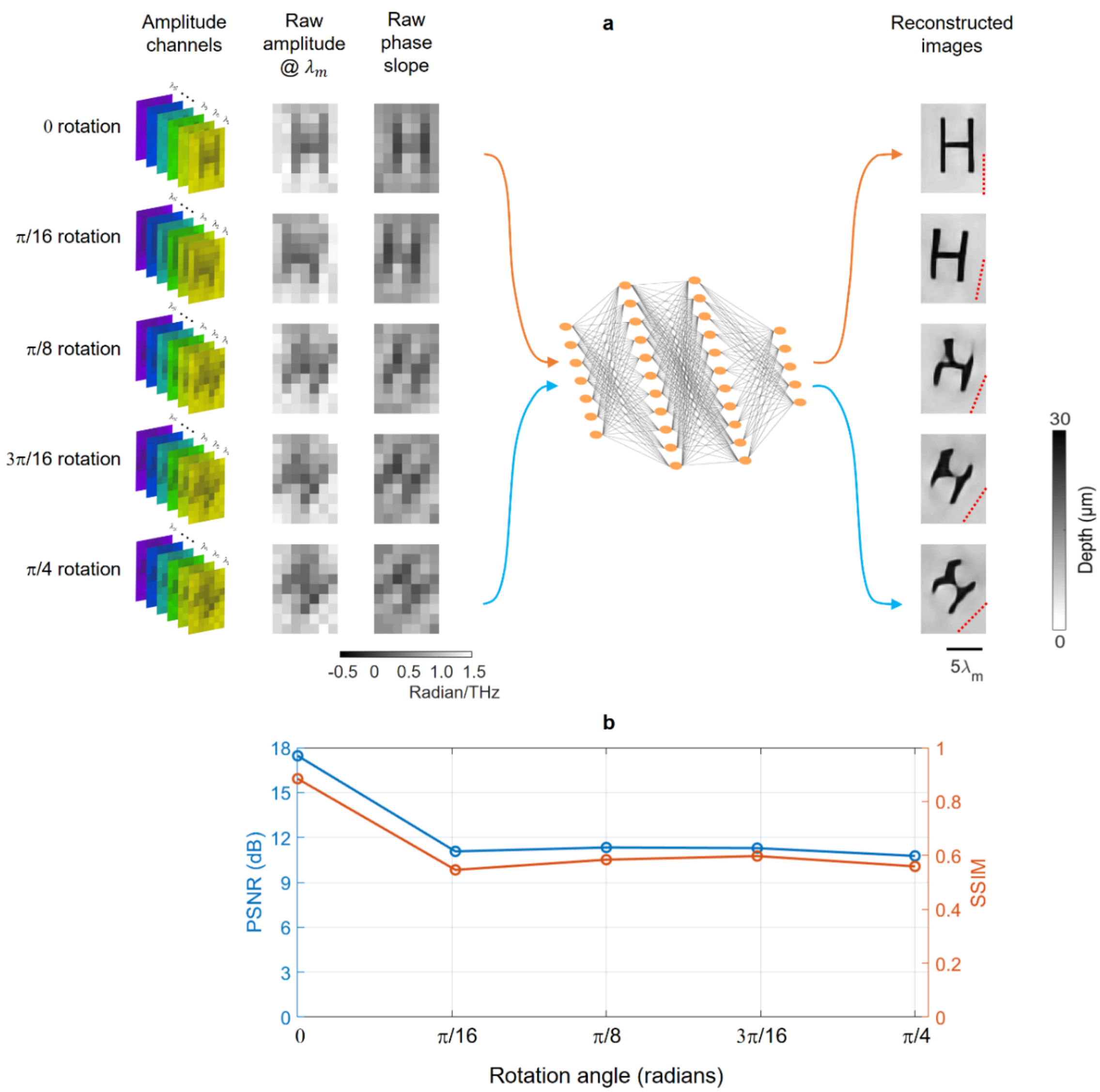

Figure S19 Rotation sensitivity analysis for the PSR-enhanced THz-FPA imaging system (shown in Fig. S5b). **a**, Reconstructed images for different experimental rotation angles inside the object plane. Although all the neural network training is performed for imaged objects placed at a zero rotation angle, the shape and depth of the objects are successfully reconstructed for rotation angles as large as π/4. **b**, The PSNR and SSIM of the reconstructed images at different rotation angles. The dashed red lines at the bottom right side of the reconstructed images are oriented along the rotation angle of the imaged object, and clearly show the success of the imaging system in preserving the orientation information of the imaged object in these blinded neural network reconstructions.

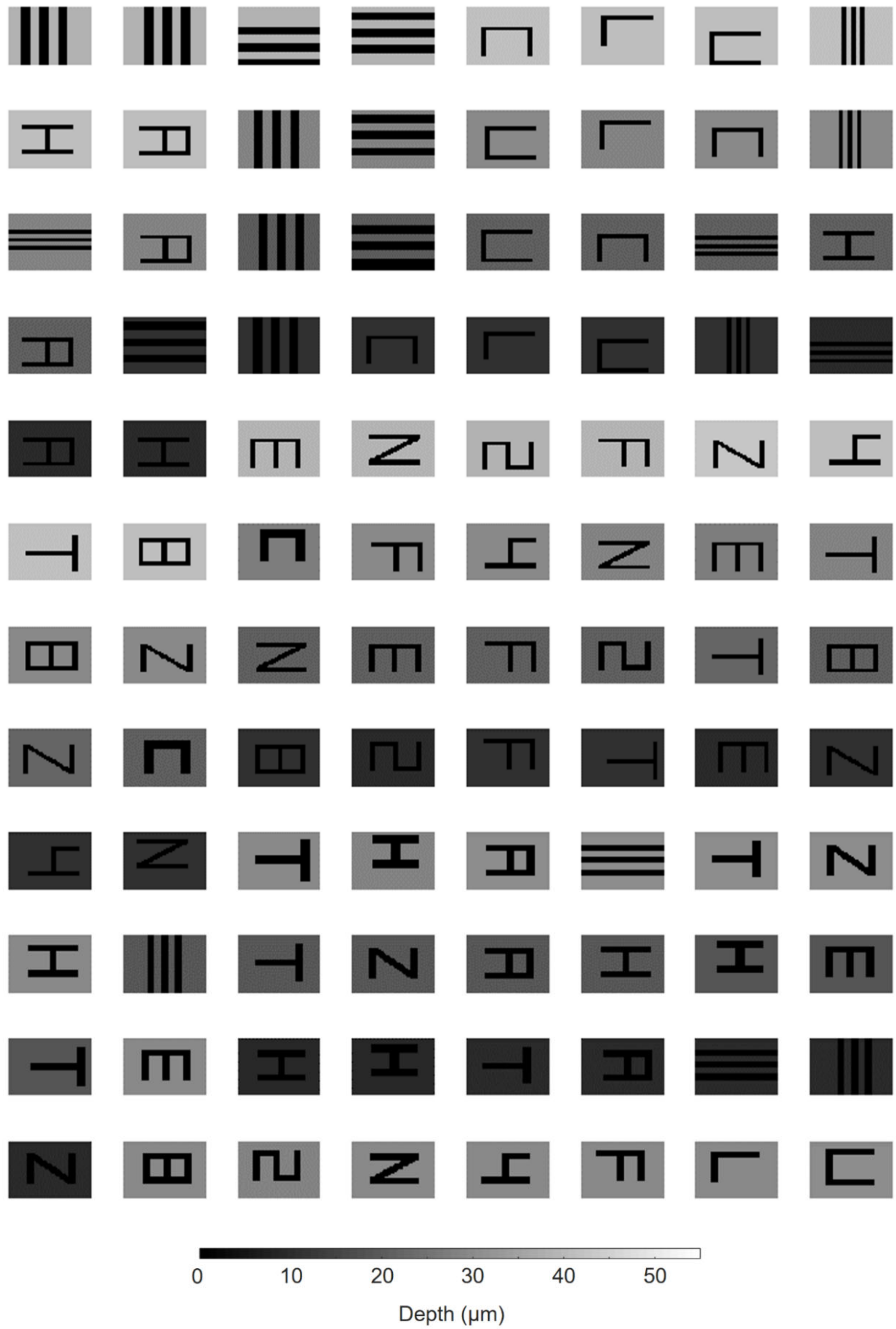

Figure S20 (1/2) Ground truth thickness images of the training set for the PSR neural network reported in Fig. 5.

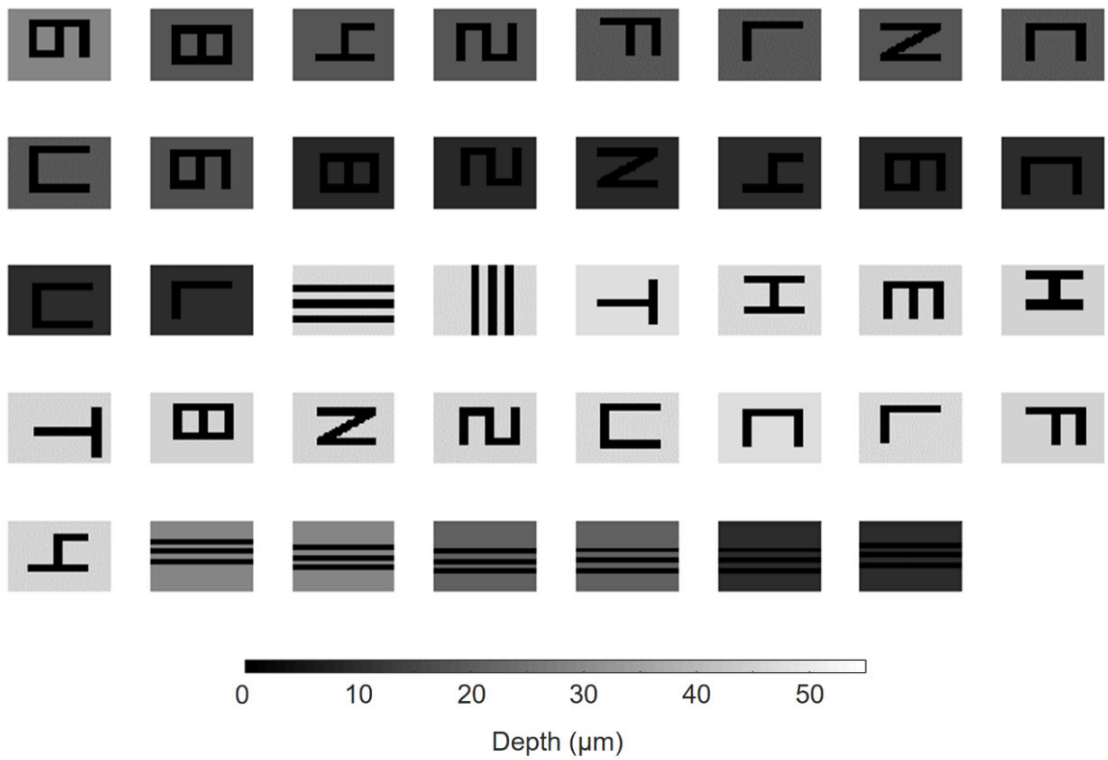

Figure S20 (2/2) Ground truth thickness images of the training set for the PSR neural network reported in Fig. 5.

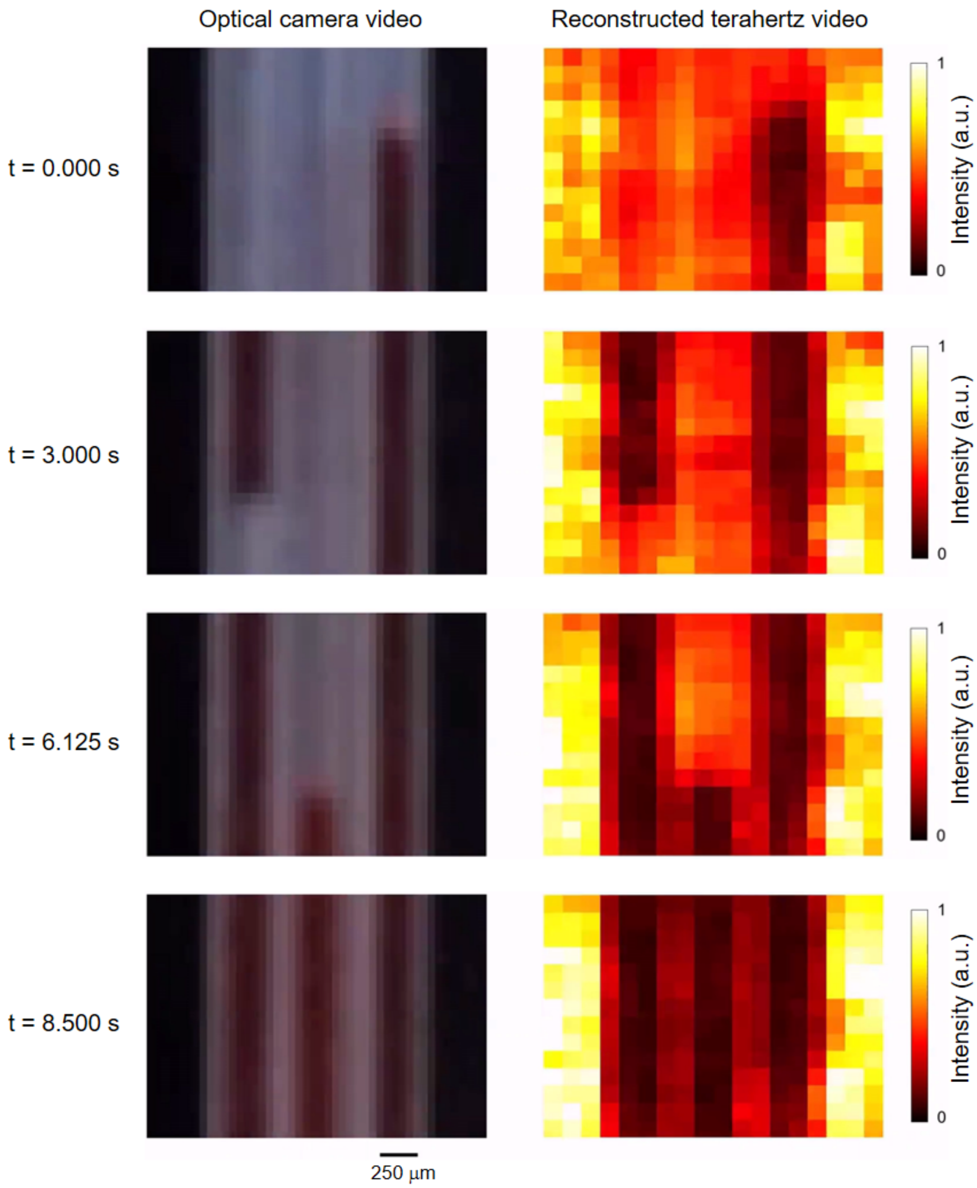

Figure S21 Holographic reconstructions of the video frames captured by the THz-FPA from water flow in adjacent plastic pipes (see Supplementary Methods and Supplementary Video for the full video). Three plastic pipes (PE tubing, World Precision Instruments) are used in this experiment with an outer/inner diameter of 500/250 µm are glued side-by-side to the backside of the THz-FPA substrate (680-µm-thick GaAs) using a 75-µm-thick sticky tape. A syringe pump is used to move water through the pipes and terahertz video frames are captured by the THz-FPA at 16 fps (for system specifications see Supplementary Fig. S8). A color (red) dye (tie dye kit, Patifeed) is added to water to better visualize its movement and an optical camera is also used to record the water flow (used only visual comparison purposes).

References

55. Nikolova, M. An Algorithm for Total Variation Minimization and Applications. *J. Math. Imaging Vis.* **20**, 89–97 (2004).

56. Herráez, M. A., Burton, D. R., Lalor, M. J. & Gdeisat, M. A. Fast two-dimensional phase-unwrapping algorithm based on sorting by reliability following a noncontinuous path. *Appl. Opt.* **41**, 7437-7444 (2002).

57. Bioucas-Dias, J. M. & Figueiredo, Má. A. T. A New TwIST: Two-Step Iterative Shrinkage/Thresholding Algorithms for Image Restoration. *IEEE Trans. Image Process.* **16**, 2992–3004 (2007).

58. Wu, Q., Hewitt, T. D. & Zhang, X. -C. Two-dimensional electro-optic imaging of THz beams. *Appl. Phys. Lett.* **69**, 1026–1028 (1996).

59. Lu, Z. G., Campbell, P. & Zhang, X.-C. Free-space electro-optic sampling with a high-repetition-rate regenerative amplified laser. *Appl. Phys. Lett.* **71**, 593–595 (1997).

60. Lu, Z. G. & Zhang, X.-C. Real-time THz imaging system based on electro-optic crystals. *in 1998 International Conference on Applications of Photonic Technology III: Closing the Gap between Theory, Development, and Applications* **3491**, 334-339, SPIE (1998).

61. Jiang, Z., Xu, X. G. & Zhang, X.-C. Improvement of terahertz imaging with a dynamic subtraction technique. *Appl. Opt.* **39**, 2982-2987 (2000).

62. Usami, M. et al. Development of a THz spectroscopic imaging system. *Phys. Med. Biol.* **47**, 3749–3753 (2002).

63. Rungsawang, R., Ohta, K., Tukamoto, K. & Hattori, T. Ring formation of focused half-cycle terahertz pulses. *J. Phys. D: Appl. Phys.* **36**, 229–235 (2003).

64. Miyamaru, F., Yonera, T., Tani, M. & Hangyo, M. Terahertz Two-Dimensional Electrooptic Sampling Using High Speed Complementary Metal-Oxide Semiconductor Camera. *Jpn. J. Appl. Phys.* **43**, L489–L491 (2004).

65. Kitahara, H., Yonera, T., Miyamaru, F., Masahiko Tani & Hangyo, M. Two-dimensional electro-optic sampling of THz radiation using high-speed CMOS camera combined with arrayed polarizers. *in Infrared and Millimeter Waves, Conference Digest of the 2004 Joint 29th International Conference on 2004 and 12th International Conference on Terahertz Electronics, 2004*. 559–560, IEEE (2004).

66. Hattori, T., Ohta, K., Rungsawang, R. & Tukamoto, K. Phase-sensitive high-speed THz imaging. *J. Phys. D: Appl. Phys.* **37**, 770–773 (2004).

67. Usami, M., Yamashita, M., Fukushima, K., Otani, C. & Kawase, K. Terahertz wideband spectroscopic imaging based on two-dimensional electro-optic sampling technique. *Appl. Phys. Lett.* **86**, 141109 (2005).

68. Yamashita, M. et al. Component spatial pattern analysis of chemicals by use of two-dimensional electro-optic terahertz imaging. *Appl. Opt.* **44**, 5198-5201 (2005).

69. Zhong, H., Redo-Sanchez, A. & Zhang, X.-C. Identification and classification of chemicals using terahertz reflective spectroscopic focal-plane imaging system. *Opt. Express* **14**, 9130-9141 (2006).

70. Hattori, T. & Sakamoto, M. Deformation corrected real-time terahertz imaging. *Appl. Phys. Lett.* **90**, 261106 (2007).

71. Spickermann, G., Friederich, F., Roskos, H. G. & Bolívar, P. H. High signal-to-noise-ratio electro-optical terahertz imaging system based on an optical demodulating detector array. *Opt. Lett.* **34**, 3424-3426 (2009).

72. Wang, X. et al. Terahertz quasi-near-field real-time imaging. *Opt. Commun.* **282**, 4683–4687 (2009).

73. Zhang, L. et al. Terahertz wave focal-plane multiwavelength phase imaging. *J. Opt. Soc. Am. A* **26**, 1187-1190 (2009).

74. Doi, A., Blanchard, F., Hirori, H. & Tanaka, K. Near-field THz imaging of free induction decay from a tyrosine crystal. *Opt. Express* **18**, 18419-18424 (2010).

75. Wang, X., Cui, Y., Sun, W., Ye, J. & Zhang, Y. Terahertz polarization real-time imaging based on balanced electro-optic detection. *J. Opt. Soc. Am. A* **27**, 2387-2393 (2010).

76. Wang, X., Cui, Y., Sun, W., Ye, J. & Zhang, Y. Terahertz real-time imaging with balanced electro-optic detection. *Opt. Commun.* **283**, 4626–4632 (2010).

77. Spickermann, G. & Bolívar, P. H. Towards a real-time electro-optical THz microscope using a demodulating optical detector array. *in CLEO:2011 - Laser Applications to Photonic Applications CThV1,* OSA (2011).

78. Blanchard, F. et al. Real-time terahertz near-field microscope. *Opt. Express* **19**, 8277-8284 (2011).

79. Doi, A., Blanchard, F., Tanaka, T. & Tanaka, K. Improving Spatial Resolution of Real-Time Terahertz Near-Field Microscope. *J Infrared Milli Terahz Waves* **32**, 1043–1051 (2011).

80. Blanchard, F., Ooi, K., Tanaka, T., Doi, A. & Tanaka, K. Terahertz spectroscopy of the reactive and radiative near-field zones of split ring resonator. *Opt. Express* **20**, 19395-19403 (2012).

81. Xie, Z. et al. Spatial Terahertz Modulator. *Sci. Rep.* **3**, 3347 (2013).

82. Clerici, M. et al. CCD-based imaging and 3D space–time mapping of terahertz fields via Kerr frequency conversion. *Opt. Lett.* **38**, 1899-1901 (2013).

83. Blanchard, F. & Tanaka, K. Improving time and space resolution in electro-optic sampling for near-field terahertz imaging. *Opt. Lett.* **41**, 4645-4648 (2016).

84. Zhao, H. et al. Metasurface Hologram for Multi-Image Hiding and Seeking. *Phys. Rev. Appl.* **12**, 054011 (2019).

85. Blanchard, F., Arikawa, T. & Tanaka, K. Real-Time Megapixel Electro-Optical Imaging of THz Beams with Probe Power Normalization. *Sensors* **22**, 4482 (2022).

86. Guerboukha, H., Nallappan, K. & Skorobogatiy, M. Toward real-time terahertz imaging. *Adv. Opt. Photon.* **10**, 843-938 (2018).

87. Brahm, A. et al. Multichannel terahertz time-domain spectroscopy system at 1030 nm excitation wavelength. *Opt. Express* **22**, 12982-12993 (2014).

88. Li, X. & Jarrahi, M. Focal-Plane Array for Terahertz Time-Domain Imaging. *in 2021 IEEE MTT-S International Microwave Symposium (IMS),* 307-310, IEEE (2021).